Experimental Thermal and Fluid Science, Volume 123, May 2021, Article number 110346
DOI: 10.1016/j.expthermflusci.2020.110346

3D Lagrangian Particle Tracking of a Subsonic Jet using Multi-Pulse Shake-The-Box

Peter Manovski[a,b,c,*], Matteo Novara[a], Nagendra Karthik Depuru Mohan[a,d,e], Reinhard Geisler[a], Daniel Schanz[a], Janos Agocs[a], Philipp Godbersen[a], Andreas Schroder[a]

[a] *Department of Experimental Methods, German Aerospace Centre (DLR), Institute of Aerodynamics and Flow Technology, Göttingen D-37073, Germany*
[b] *Aerospace Division, Defence Science and Technology Group, Victoria 3207, Australia*
[c] *Department of Mechanical Engineering, University of Melbourne, Victoria 3010, Australia*
[d] *Department of Engineering, University of Cambridge, Cambridge CB2 1PZ, United Kingdom*
[e] *Centre for Defence Engineering, Cranfield University, The Defence Academy of the United Kingdom, Shrivenham SN6 8LA, United Kingdom*

Abstract

Three-dimensional (3D) Lagrangian Particle Tracking (LPT) was performed on a subsonic jet flow at Mach 0.506 and 0.845 generated by a round nozzle with diameter-based Reynolds numbers of 1.7×10^5 and 3.1×10^5, respectively. The Multi-Pulse Shake-The-Box (MP-STB) technique was employed to reconstruct particle tracks along the four-pulse sequences, which were obtained by using orthogonally polarised light to separate the pulses on camera images. The MP-STB method applied here has a number of differences compared to previous publications, in particular, a new adaptive search radii approach and an iterative strategy and particle track validation criteria that have been customised for high subsonic/transonic flows. A description of this methodology is given followed by presentation of the instantaneous 3D flow velocity and material acceleration particle tracks. By ensemble-averaging the scattered instantaneous measurements extracted from individual particle tracks into small volumetric bins, highly resolved statistical quantities were obtained. The performance of MP-STB was assessed by comparing velocity profiles with published particle image velocimetry (PIV) data-sets. MP-STB was better able to resolve the steep velocity gradients, in particular the thin jet shear layer near the nozzle exit. At this location the MP-STB results also yielded higher turbulence intensities compared with the reported studies for similar flow conditions. The MP-STB acceleration flow statistics were compared for the two Mach numbers, and for the Mach 0.506 case, higher levels of normalised acceleration and fluctuations were found. The position accuracy of the 3D imaging system was quantified and it was found that the use of two different states of polarisation had a direct impact on the accuracy and the amount successfully tracked particles. Further assessment of the particle imaging quality of each camera revealed a significant disparity between cameras. This was attributed to the particle light scattering intensity variations, which were highly dependent on the particle size, camera angles and different states of polarised light. Despite these challenges, an average of 40,000 individual particle tracks could be reconstructed from a typical particle image density of 0.02 particles per px (and an active sensor area of 1800×2200 px^2). Furthermore, the accuracy of the measurement was shown to be relatively high, with respect to PIV.

Keywords: Jet, Lagrangian Particle Tracking, Particle Image Velocimetry, Shake-The-Box, Shear Layer

1. Introduction

Jet flows and their radiated noise are classical fluid mechanics and aeroacoustic research topics that remain of high interest. The high subsonic jet flow from a typical commercial aircraft engine exhaust emanates significant noise, and is one of the main components of aircraft noise, particularly at take-off. Significant efforts have been made to understand, predict and mitigate the level of (such) jet noise in order to reduce the environmental impact and to meet future airport regulations. A key to understanding jet noise and the source mechanisms is the ability to measure the velocity fields with high spatial resolution (Morris, 2011; Bridges and Wernet, 2012). For more than a decade a large number of researchers have investigated high subsonic jet flows using planar two-dimensional two-component Particle Image Velocimetry (2D/2C PIV) or two-dimensional three-component stereoscopic PIV (2D/3C SPIV), see Arakeri et al. (2003); Alkislar et al. (2007); Fleury et al. (2008); Tinney et al. (2008); Bridges and Wernet (2011); Morris (2011); Henning et al. (2013); Fontaine et al. (2015); Brés et al. (2018), and references therein. These techniques allow the capture of instantaneous jet flow fields and turbulent statistics in a 2D plane, typically at moderate spatial resolutions. To date, there have only been a limited number of studies investigating these high subsonic jet flows with three-dimensional (3D) or volumetric measurement techniques and only one (Sellappan et al., 2020) reported thus far with Lagrangian particle tracking (LPT), which can generally provide higher spatial resolution than typical PIV methods (Kähler et al., 2012a; Schröder et al., 2015). The current study aims to demonstrate a new adapted version of a recently developed 3D LPT algorithm, namely, Multi-Pulse Shake-The-Box (MP-STB) (Novara et al., 2016b) and show-

*Corresponding author
Email address: Peter.Manovski@dst.defence.gov.au (Peter Manovski)

case the potential of the technique to provide new insights into jet flow physics by revealing highly resolved 3D jet flow velocity and acceleration fields, and their statistical quantities.

An established technique to obtain three-component velocity fields in 3D domains (3C/3D) is Tomographic-PIV (Tomo-PIV), see Scarano (2013) who provides a detailed review. Tomo-PIV has been applied to a low Reynolds number jet flows, such as in Staack et al. (2010); Violato and Scarano (2011, 2013); Wernet (2017), however its application to high subsonic jet flows is still limited, with Wernet (2016), the only published paper in the open literature to-date. In the study by Wernet (2016), the desire for volumetric measurements was to obtain all three components of vorticity in the jet flow field and potentially reduce the number of measurement configurations (streamwise and cross-stream) that are typically required to characterise flows from different nozzles. As quantifying the uncertainty in Tomo-PIV is difficult, Wernet (2016) compared its performance against well established PIV techniques (2D/2C PIV and 2D/3C SPIV). For a jet flow condition of Mach (M) 0.9, Wernet (2016) also compared the Tomo-PIV data with the 'consensus' data-set by Bridges and Wernet (2011). The consensus data-set was obtained by weighted averages from six historical PIV data-sets, while exploiting the axial symmetry of the flow and has been extensively used for validation of computational jet flow simulations, see Bridges and Wernet (2012), and references therein. In the case of Tomo-PIV, the data generally agreed well with the 2D/2C PIV, 2D/3C SPIV and the consensus data-set, however, large deviations were noted in the shear layer near the nozzle exit. These discrepancies were attributed to the very thin shear layer, and the PIV interrogation window size which was of the same order as the shear layer thickness and thus inadequately resolved by the Tomo-PIV technique. It should be noted that, the near nozzle region of the flow is of high interest, as it influences noise generation and turbulence levels further downstream of the jet (Fontaine et al., 2015).

Lagrangian particle tracking methods (also commonly referred to as Particle Tracking Velocimetry - PTV) have been shown to alleviate such spatial averaging effects and outperform PIV (Kähler et al., 2012a). In Kähler et al. (2012a) the response of synthetic particle image data was investigated for a simulated step-change velocity profile, which is directly applicable to jet flow as a similar velocity distribution is seen near the nozzle exit. In their study, the position of the steep change in displacement was captured best by the PTV algorithm. The window-correlation method used in PIV could not correctly respond to the step profile and led to a broad response, that was dependent on the interrogation window size and particle image size, therefore limiting the spatial resolution. The PTV evaluation did not have the same limits, it achieved better resolution and agreement with the reference velocity. PTV/LPT has seen use in a broad range of applications although its application in jet flows has been limited. Kim et al. (2016) is one such study that used 3D-PTV to characterise the flow of low Reynolds number circular and semi-circular jets. In that study around 500 particles tracks were detected in each instantaneous realisation, with 30,000 and 144,000 images taken in two separate experiments. The PTV approach allowed a Lagrangian statistical description of the flow, including the mean particle accelerations and the standard deviation of the accelerations.

Dual-plane or four-pulse PIV methods can also increase the accuracy and the dynamic range of a measurement, as well as allowing the out-of-plane velocity gradients and accelerations to be determined. Kähler and Kompenhans (2000) used this approach with the flow field illuminated by orthogonally polarised light from four lasers to avoid multiple exposed particle images. This study was followed by Perret et al. (2006), who measured the three components of acceleration using dual-plane SPIV. Similarly, Mullin and Dahm (2006) obtained the velocity gradient tensor and provided a detailed accuracy assessment of their method. More recently, the approach was extended to 3D with four-pulse Tomo-PIV using two independent imaging systems (each with four cameras) by Schröder et al. (2013) and a 12-camera Tomo-PIV system by Lynch and Scarano (2014). In the current study we combine the advantages of LPT and four-pulse methods by using Multi-Pulse Shake-The-Box. The STB method for time-resolved (TR) applications is described in Schanz et al. (2016) and allows for accurate 3D LPT of densely seeded (>0.08 particles per pixel, ppp, Huhn et al., 2017) flows, however, due to current limitations of camera and illumination hardware it is typically limited to low speed flows <20-40 m/s in air. Novara et al. (2016a), showed that a short time sequence (or multi-pulse) implementation of STB was able to retrieve most particle tracks with velocity and acceleration dynamic ranges comparable to those obtained with TR-STB, and they suggested the method can be used to measure the material acceleration for high-speed flows. Subsequently, the method was used in turbulent boundary layer investigations with a free-stream velocity up to 36 m/s (Novara et al., 2016b, 2019). In their latest study (Novara et al., 2019), MP-STB provided a resolution of one-third of a wall unit (equivalent to 0.5 px), with mean and fluctuating velocity statistics that were within 1% and 2% of Direct Numerical Simulations (DNS), thereby demonstrating the ability of the MP-STB technique to accurately measure and resolve the viscous layer. In a very recent paper by Sellappan et al. (2020), a variant of MP-STB with multi-exposed particle images was used to characterise the 3D flow of free and impinging jets at M 0.31 and M 0.59. In that study, particle track counts of up to 26,000 were obtained (for a nominal particle image density of 0.08 ppp and a reconstruction volume of $117 \times 80 \times 12.5$ mm^3). Eulerian statistics were obtained using the VIC# data assimilation method and the mean axial profiles and normalised vorticity results were found to compare well with planar PIV, SPIV and Tomo-PIV of the same flow. For each case in that study only a small number of images (450) were acquired and processed, as such the ability of MP-STB to provide high resolution ensemble-averaged statistical quantities was not explored, similarly the velocity fluctuations and acceleration measurements were not quantitatively examined. These aspects as well as others will be explored in the current paper.

The application of MP-STB in jet aeroacoustics offers the potential to an accurate means of establishing a direct correlation between the flow dynamics in the jet near field and the acoustic pressure fluctuations in the far field. Ultimately, the

pressure in the near field is the desired quantity to determine the sources of aeroacoustic noise. The pressure field can be indirectly obtained via non-intrusive optical flow measurements of the material acceleration by PIV (van Oudheusden, 2013). The pressure is typically obtained by spatial integration of the momentum equation and for turbulent flows at high Reynolds number, the viscous term has been shown to be negligible leaving the material acceleration to dominate and thus the most important measurement quantity (van Oudheusden, 2013; Huhn et al., 2018). In another recent paper by van Gent et al. (2017), a comparison of a range of techniques for pressure reconstruction showed that the accuracy can be significantly improved by using STB where the material acceleration is obtained directly from individual particle trajectories. The accuracy of PIV and STB for both time-resolved (TR) and multi-pulse input data was assessed. The TR-STB showed the lowest global error, the next best was MP-STB (1.6× larger error) followed by TR-PIV and two-pulse PIV which showed higher errors (2× and 4×, respectively). This positive outcome for MP-STB has provided further motivation in the current study to measure the material acceleration with this method. Following the successful validation of the MP-STB processing techniques on synthetic data by Novara et al. (2016a) and van Gent et al. (2017), this experimental investigation will also serve to provide further validation and assessment in real experimental conditions.

In this work we apply MP-STB on circular jet flow at two Mach numbers to reveal Lagrangian and Eulerian statistical velocity and acceleration fields. The details of the experimental set-up is described in Section 2, then the MP-STB particle tracking approach for four-pulses is detailed in Section 3. The main results are presented and discussed in Section 4. A discussion is made on the validation criteria in Section 5 and an assessment of the particle imaging quality is provided in Section 6. Concluding remarks are made in Section 7 and an estimate of the measurement uncertainty is provided in Appendix A.

2. Experimental set-up

The experiment was carried out in the anechoic aeroacoustics test facility at the German Aerospace Center (DLR) Göttingen. The jet flows issued by a round nozzle with an inner diameter, D_j, of 15 mm and lip thickness of 3 mm was investigated. The nozzle geometry, including the inner contour which follows a seventh order polynomial, are described in Miguel and Henning (2013). An image of the nozzle and inner profile are shown in Fig. 1.

Two jet flow Mach number (M) conditions of M 0.506 and M 0.845 were investigated. Where M is defined as the jet centreline velocity normalised by the ambient speed of sound. For each case, the Reynolds number based on the nozzle diameter (Re_{D_j}) was 1.7×10^5 and 3.1×10^5, respectively. The ratio of stagnation pressure in the jet to the nozzle ambient pressure was measured by a differential digital manometer (Greisinger GDH-14A). The ratio of the stagnation temperature of the jet to the nozzle ambient temperature was measured using a thermocouple (RS Pro Thermoelement Type K). The experimental

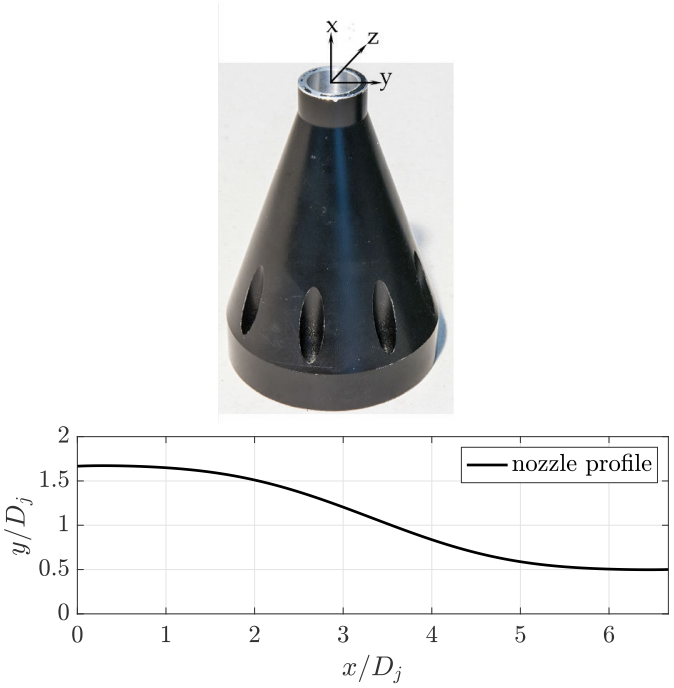

Figure 1: Top: image of round nozzle and Cartesian co-ordinate system. Bottom: inner profile of nozzle with inner diameter, D_j = 15 mm.

parameters and flow conditions are summarised in Table 1 and 2.

A multi-pulse setup was obtained by the combination of two dual-frame acquisition systems to record tracer particle images within a volume of 90×70×10 mm^3 along the jet axial (x), lateral (y) and out-of-plane (z) directions, respectively. The multi-pulse acquisition strategy described by Schröder et al. (2013) and Novara et al. (2016b) is applied here, where the use of two different states of polarisation for the illumination sources is used to separate the pulses on the camera images.

Illumination is provided by two dual-cavity Quantel Evergreen Nd:YAG lasers and two dual-cavity Big Sky CFR400 Nd:YAG lasers (each with 200 mJ pulse energy at 10 Hz) emitting parallel and perpendicular polarised light respectively to produce short four-pulse bursts. To increase the available laser energy each pulse of the Evergreen lasers is combined with a pulse from the CFR400 lasers, resulting in a total energy per pulse of approximately 400 mJ. The laser sheet was also back reflected with a flat mirror to further increase the illumination intensity of particles and to provide more symmetric scattering directions for the particle images of both camera systems. The layout of the four dual cavity lasers is shown in Fig. 2, as well as the optical arrangement used to produce the volumetric light sheet at the nozzle.

The timing scheme of the four lasers is arranged to enable a four-pulse sequence, where the time separation between pulses 1 and 2, and that between pulses 3 and 4, is kept the same and a longer time interval (3 × pulse separation of pulses 1-2 and 3-4) between pulses 2 and 3 (see Table 2). The motivation for the chosen pulse separation is to increase the velocity and ac-

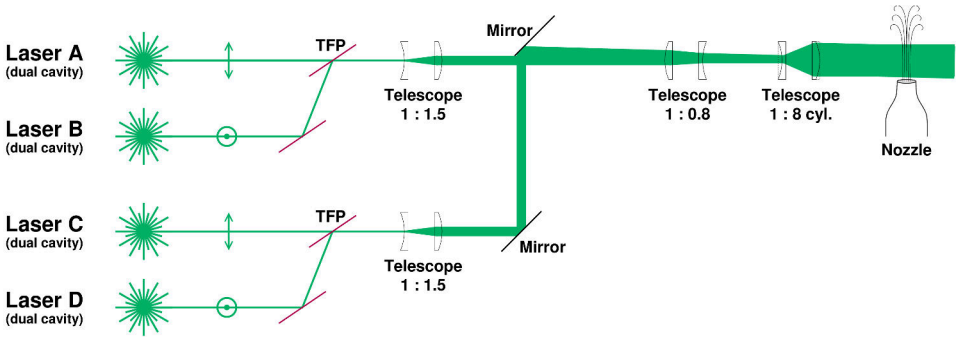

Figure 2: Laser illumination set-up consisting of four dual cavity lasers (A-D). TFP: Thin Film Polariser. Perpendicular polarised light (↕) and parallel polarised light (⊙). Lasers B and D produce pulses 1-2, whereas Lasers A and C produce pulses 3-4.

celeration dynamic ranges of the measurement. Experimental conditions, with real imaging effects and seeding variability are expected to make the particle tracking process more challenging, as a result a more conservative separation distance between the second and third pulses was taken compared to Novara et al. (2016b) and van Gent et al. (2017), who used 4 × pulse separation of pulses 1-2 and 3-4.

The two imaging systems are shown in Fig. 3, each consist of four sCMOS PCO-Edge cameras, all equipped with polarisation filters to separate the four pulses onto the image sensor. One imaging system (odd camera numbers in Fig. 3) records pulses 1 and 2 and the other (even camera numbers) pulses 3 and 4. The sensor size is 2560×2160 pixel with a pixel pitch of 6.5 μm. Cameras, in Scheimpflug condition, are equipped with objective lenses having a focal lengths of f = 200 mm and 180 mm; the f-number ($f_\#$) was set to 11. The average digital resolution was approximately 33.63 px/mm and was computed in the centre of the volume and averaged over the camera set. As a consequence of the uneven spacing of the pulses, the maximum displacement of particle tracers is approximately 13 px and 39 px for the shorter and longer time interval respectively, resulting in a total maximum particle shift of approximately 65 px.

An aerosol generator with an impactor was used to provide seeding of Di-Ethyl-Hexyl-Sebacat (DEHS) with a nominal particle diameter of 1 μm. The relaxation time of DEHS particles of this size is approximately 2 μs, as was measured experimentally by Ragni et al. (2011), over an oblique shock at Mach 2. Given in that study DEHS performed well, it can be considered an adequate tracer particle to follow high subsonic flow faithfully. The seeding was introduced upstream of the nozzle and the ambient air was also seeded to enable a near homogenous distribution across the measurement volume. However, perfect homogeneity was difficult to achieve and generally the jet core exhibited a slightly higher seeding density compared to the ambient flow. The symmetric camera set-up ensured similar image quality between the two acquisition systems. The seeding concentration adopted for the experiment resulted in a particle image density of approximately 0.015-0.03 ppp.

The two imaging systems are calibrated using a LaVision Type-11 two-plane target; volume self-calibration Wieneke (2008) is used to compensate for calibration errors and to obtain the Optical Transfer Function (OTF) of the particle images (Schanz et al., 2013). The self-calibration images of low seeding density were obtained with all lasers (A-D) fired simultaneously. This allowed a single volume self-calibration to be performed (Schröder et al. (2013); Lynch and Scarano (2014)) as well as an independent volume self-calibration, where the odd and even camera systems were calibrated independently. The differences between the two calibration methods was minimal and the independent volume self-calibration was adopted. Calibration errors were of the order of 0.1 px or less than 3 μm in physical space.

For the M 0.506 measurement configuration, a total of 45,000 four-pulse sequences were recorded at a sampling frequency of 10 Hz. For the M 0.845 case, a total of 60,000 four-pulse sequences were recorded at 10 Hz.

Table 1: Experimental parameters (where D_j = 15 mm). See Appendix A for details on how the velocity and acceleration dynamic ranges were calculated.

Measurement volume	$70 \times 90 \times 10$ mm^3
Measurement domain	$0.1{\times}D_j$ to $4.6{\times}D_j$
Dynamic spatial range	≈ 1,500:1
	(for one-point statistics)
Dynamic velocity range	≈ 224:1
Dynamic acceleration range	≈ 16:1
Observation distance	≈ 900 mm
Recording method	dual frame/single exposure
Recording medium	8 PCO.edge sCMOS
	2560×2160 pixel
Recording lens	f = 180 mm, $f_\#$=11 and
	f = 200 mm, $f_\#$=11
Average Pixel Resolution	33.63 px/mm
Illumination	4 Nd:YAG laser 200 mJ/pulse
Seeding material	DEHS droplets ($d_p \approx 1$ μm)

3. Lagrangian particle tracking with Shake-The-Box

A version of the Shake-The-Box 3D LPT algorithm, initially proposed by Schanz et al. (2016) for time-resolved recordings, is adapted here to four-pulse sequences (similar to Novara et al., 2016b). An iterative STB processing strategy is employed to

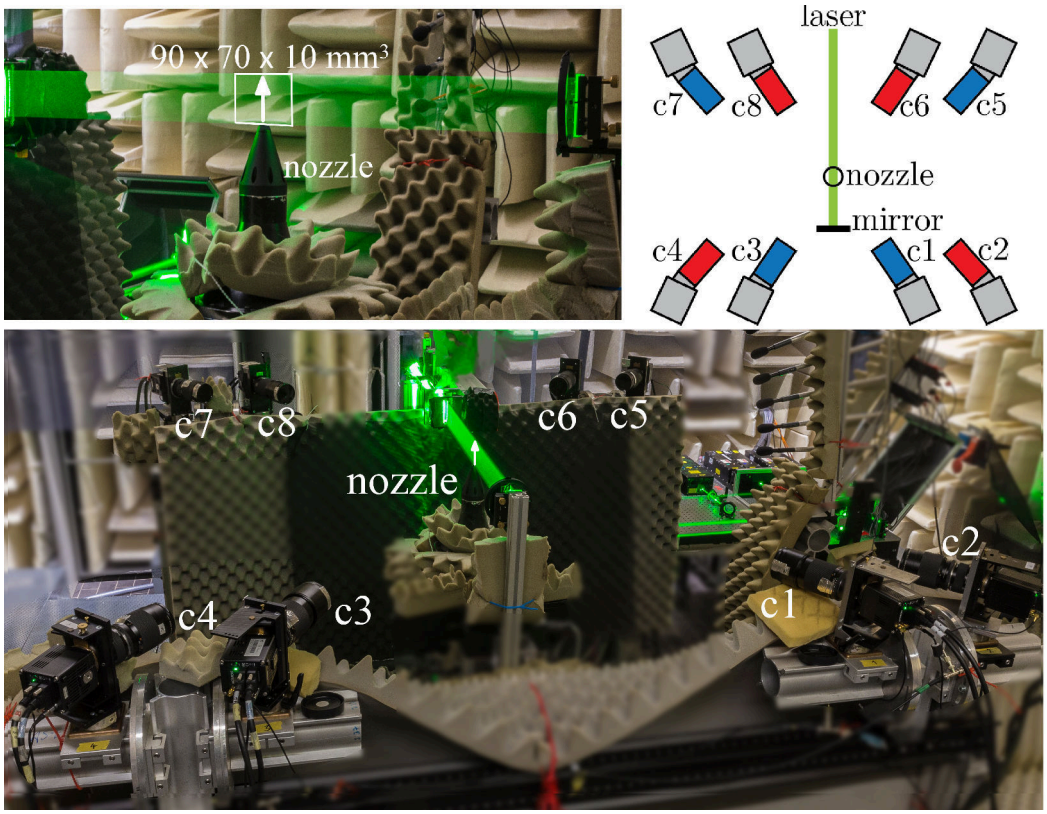

Figure 3: Top-left: a photograph of the jet apparatus showing the jet flow direction, laser light sheet and measurement volume. Top-right: a schematic diagram (not-to-scale) showing a plan-view of the in-line camera set-up with two imaging systems each with four cameras separated by two states of polarisation (indicated by the odd and even camera numbers). Bottom: a photograph of the experimental set-up.

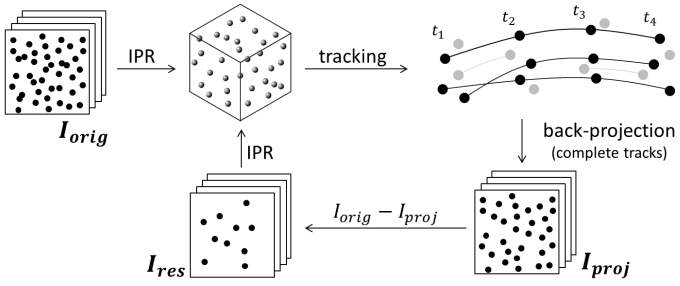

Figure 4: Iterative MP-STB processing strategy for four-pulse sequences (adapted from Novara et al., 2016a).

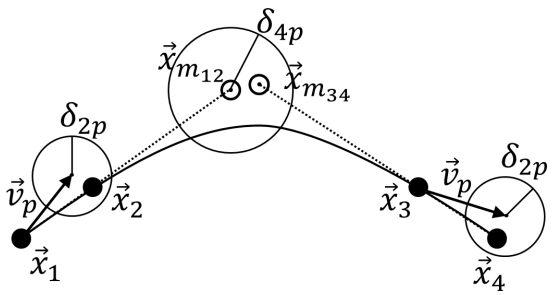

Figure 5: Particle tracking strategy for uneven pulse separation; $\vec{x}_i$ indicates the position of the particles along the four-pulse sequence (adapted from Novara et al., 2016a).

compensate for the lack of a long sequence of time-resolved data. The number of STB iterations, as well as the reconstruction and tracking parameters, is chosen based on the image quality, seeding density and pulse separation arrangement. For the present investigation four STB iterations have been performed for each four-pulse recording sequence. The Iterative Particle Reconstruction technique (IPR, Wieneke, 2013) and the particle tracking parameters are summarised in Table 3, where N_c indicates the number of cameras within each imaging system. A detailed description of the reconstruction and tracking strategy and parameters can be found in Wieneke (2013);

Novara et al. (2016a,b).

The processing strategy is depicted in Fig. 4. Initially, the recorded images (I_{orig}) are reconstructed in three-dimensions via IPR to triangulate and correct ('shake') particles for each of the four pulses. Next the particle matching procedure employed for the tracking phase is divided into two stages (with reference to Fig. 5). At first, two-pulse tracks between pulses 1-2 and 3-4 are identified; around each particle in the first time step (pulse 1 and 3 respectively) a radius is established to define a search area where matching particles from the second step (pulse 2 and 4) are identified. This step is aided by the use of instantaneous velocity predictors obtained by means of Particle Space Correlation (PSC, Novara et al., 2016a) performed between IPR reconstructed particle fields ($\vec{v}_p$ in Fig. 5). The use of such a predictor allows for the reduction of the search radius thereby improving the identification of valid particle tracks (Novara and Scarano, 2013).

The second stage of the tracking process is to obtain four-pulse tracks by connecting two-pulse tracks that have been identified. This is done by determining the position of the particles at the mid-point of the four-pulse sequence by extrapolating the two-pulse tracks from pulses 1-2 forward and 4-3 backward in time respectively ($\vec{x}_{m_{12}}$ and $\vec{x}_{m_{34}}$ in Fig. 5). A search radius, δ_{4p} is established to define the area within which the predicted mid-points need to be found for the two-pulse tracks belonging to pulses 1-2 and 3-4 to be connected into four-pulse tracks.

The search radii, δ_{2p} and δ_{4p} are referred to as global radii; and their value is kept constant across the measurement domain and does not depend on local flow features. If an estimate of the velocity fluctuation components is available, the global search radii can be locally adapted according to the standard deviation of the velocity to obtain the local radii:

$$\delta^*_{2p} = \delta_{2p} + f_{\sigma,2p} \times \sigma, \tag{1}$$

$$\delta^*_{4p} = \delta_{4p} + f_{\sigma,4p} \times \sigma, \tag{2}$$

where σ indicates the standard deviation of the velocity in pixels and $f_{\sigma,2p}$ and $f_{\sigma,4p}$ are positive multiplicative factors that can be freely adjusted. Such adaptive search radii enables an increase of the search area in regions where high flow dynamics are expected, therefore allowing the capture of high acceleration events; conversely, the search area is reduced in the calm region outside the jet, where an average velocity predictor is accurate enough to aid the particle matching procedure.

Table 2: Flow conditions and laser pulse delay time

Mach number (M)	0.506	0.845
Jet exit axial velocity	173.8 m/s	290.6 m/s
Reynolds number (Re_{D_j})	1.7×10^5	3.1×10^5
Nozzle pressure ratio	1.19	1.72
Nozzle temperature ratio	1.0	0.98
Total 4-pulse sequences	45,000	60,000
Pulse delay 1-2 and 3-4	2.25 μs	1.25 μs
Pulse delay 2-3	6.75 μs	3.75 μs

After evaluation of the 4-pulse tracks is completed, a second degree polynomial regression is used to fit the particle positions along the track in time and the average deviation from the fit is computed as:

$$\varepsilon_{fit} = \left| \frac{1}{N_p} \sum_{i=1}^{N_p} \sqrt{(\vec{x}_{i,p} - \vec{x}_{i,fit})^2} \right|. \tag{3}$$

Here $\vec{x}_{i,p}$ indicates the reconstructed particle position at each time instant, $\vec{x}_{i,fit}$ is the position of each particle resulting from the second order polynomial fit and N_p equals the number of pulses. In the case of two or more track candidates that have one or more particles in common, the one with the lowest value of ε_{fit} is chosen, while the others are discarded. If the average deviation for a track is larger than a threshold value (ε^*_{fit}, listed in Table 3), the track candidate is also discarded. Particles that could not be tracked over the complete four-pulse sequence are rejected (grey dots in Fig. 4). This ensures that spurious ghost particles arising from the reconstruction process, typically not coherent with the flow motion, are discarded (Elsinga et al., 2011; Novara et al., 2016a). Less than 1% ghost tracks were detected by Novara et al. (2016b) on synthetic data with one imaging system. The chance of producing ghost tracks is further reduced by the use of two independent imaging systems (Discetti et al., 2013).

After these steps, the retained particles are back-projected onto the image plane for each time instant to form projected images (I_{proj}); these are subtracted from the original recordings (I_{orig}) to obtain residual images (I_{res}). These steps constitute a single STB iteration (one loop in Fig. 4; the images of particles which have not been reconstructed by IPR (e.g. due to situations of particle image overlap) or failed to be matched during tracking (e.g. due to inaccuracy of predictor or inadequate search radius) remain in the residual images. These residual images are then used to perform further STB iterations. Depending on the number of tracks successfully reconstructed in the previous iteration(s), the residual images will exhibit a lower particle image density, therefore offering a less complex reconstruction and tracking problem enabling the recovery of previously undetected particles. The lower values of the search radii and allowed deviation from fit (ε^*_{fit}) for the first STB iteration ensure that only the most reliable tracks are initially identified. After these particles have been subtracted from the recorded images, more challenging tracks (e.g. exhibiting higher noise or higher accelerations) can be identified by gradually relaxing the partner search and allowed deviation from fit parameters. Table 3 indicates that the allowed deviation from fit (ε^*_{fit}) was relaxed further in the case of M 0.506 compared to M 0.845. These values were chosen based on the image quality, seeding density, pulse separation arrangement, visual inspection of the acceleration fields and the percentage of discarded tracks, which was less than $\approx$ 2% of total tracks for both cases. Finally, once all STB iterations are completed the particle velocity and acceleration are determined analytically from the quadratic fit, hence the double differentiation results in a constant acceleration over

Table 3: MP-STB processing parameters for the evaluation of the complete sequence of recordings

	iteration 1	iteration 2	iteration 3	iteration 4
Triangulations with N_c	3	3	3	3
Triangulations with N_{c-1}	2	2	2	2
IPR shake iterations	4	4	4	4
Shake width [px]	0.1	0.1	0.1	0.1
Allowed triangulation error [px]	1.2	1.2	1.2	1.2
Particle peak intensity threshold [counts]	40	40	40	40
Particle peaks used for triangulation η [%]	100	100	100	100
Projection factor prior to triangulation	2.5	2.5	2.5	2.5
Global search radius 2-pulse tracks δ_{2p} [px]	0.2	0.3	0.4	0.5
Search radius 2-pulse mult. factor $f_{\sigma,2p}$	2	3	4	4
Global search radius 4-pulse tracks δ_{4p} [px]	0.4	0.6	0.8	1.0
Search radius 4-pulse mult. factor $f_{\sigma,4p}$	3	4.5	6	6
M 0.506 maximum deviation from fit (2^{nd} poly.) ε^*_{fit} [px]	0.5	0.7	1.1	1.3
M 0.845 maximum deviation from fit (2^{nd} poly.) ε^*_{fit} [px]	0.5	0.6	0.7	0.9

the four-pulse sequence. The midpoint position of the sequence is chosen for the evaluation from the fit as it provides the best accuracy (Gesemann et al., 2016).

3.1. Application of Multi-Pulse STB

Prior to the application of MP-STB, image pre-processing consisted of subtracting a constant value ($\approx$ 310 counts) from each camera image to reduce the influence of background image noise and increase the signal-to-noise ratio. The effectiveness of MP-STB relies heavily upon a high fidelity velocity predictor with converged flow statistics at sufficient resolution to capture the gradients in the flow field. As such, we followed a staged approach by progressively increasing the resolution of the predictor and the sample size. Firstly, a small batch of 200 four-pulse sequences was evaluated using the PSC method (Novara et al., 2016a). The processing parameters for PSC consisted of two passes with the initial interrogation volume size of 96 px^3 and the final pass with an interrogation volume of 48 px^3, both with 50% overlap. The corresponding peak detection search radii for each pass were 16 px and 8 px, respectively. The PSC field was then averaged to provide a mean flow field as a predictor for the subsequent MP-STB evaluation.

Using the averaged PSC flow field as a velocity predictor, a batch of 4,000 four-pulse sequences was then evaluated using MP-STB. As no reliable information on the flow statistics was available, both $f_{\sigma,2p}$ and $f_{\sigma,4p}$ in Eq. (1) and Eq. (2) were initially set to zero. Whereas, the global search radii were respectively increased after each STB iteration (δ_{2p} = 2, 3, 4, 4 px and δ_{4p} = 4, 5, 6, 6 px) taking advantage of the progressive reduction in the residual image density and allowing for the identification of previously unidentified particle tracks (Novara et al., 2016b).

The first MP-STB ensemble-averaged flow field results were then obtained by bin-averaging of the scattered 3D particle track data into small volumetric bins as proposed in Schröder et al. (2015) and Novara et al. (2016b). The bin size chosen here was 30 px ($0.06 \cdot D_j$), 10 px ($0.02 \cdot D_j$) and 10 px ($0.02 \cdot D_j$) in the axial (x), lateral (y) and out-of-plane (z) directions, respectively. This process was then repeated with a larger batch of 10,000 four-pulse sequences. The resulting bin-average was then used as a predictor for the STB evaluation of the total four-pulse sequences of 45,000 (M 0.506) and 60,000 (for M 0.845). For each of the four STB iterations the global search radii were reduced (see Table 3) and locally adapted according to the velocity fluctuation magnitude as shown in Eq. (1). The adaptive factors ($f_{\sigma,2p}$ and $f_{\sigma,4p}$) were progressively increased at each STB iteration ensuring that by the final (fourth) pass events up to four times the local expected displacement standard deviation could be captured.

In the present work, the particle position, velocity and acceleration are sampled at the temporal mid-points of the track for the ensemble averaging and corresponding higher-order one-point statistics in a fast classical binning approach. A more recent development by Godbersen and Schröder (2020) uses weighted functional binning, which exploit the full available information along all tracks, enhancing convergence speed and as well as providing direct uncertainty quantification but at the expense of more computational effort.

4. Results

From a typical particle density of 0.02 ppp (for an active sensor area of 1800 x 2200 px^2) an average of 40,000 particle tracks could be successfully reconstructed for each instantaneous four-pulse recording sequence. Depending on the seeding density and individual camera image quality, instances of up to 60,000 particle tracks were recorded. It should be noted that the number of tracks refers to complete four-pulse tracks only; particles entering or leaving the investigated domain are not considered for sake of robustness of the measurement.

The experimental instantaneous flow field results for the round jet at M 0.845 are presented in Section 4.1. The mean

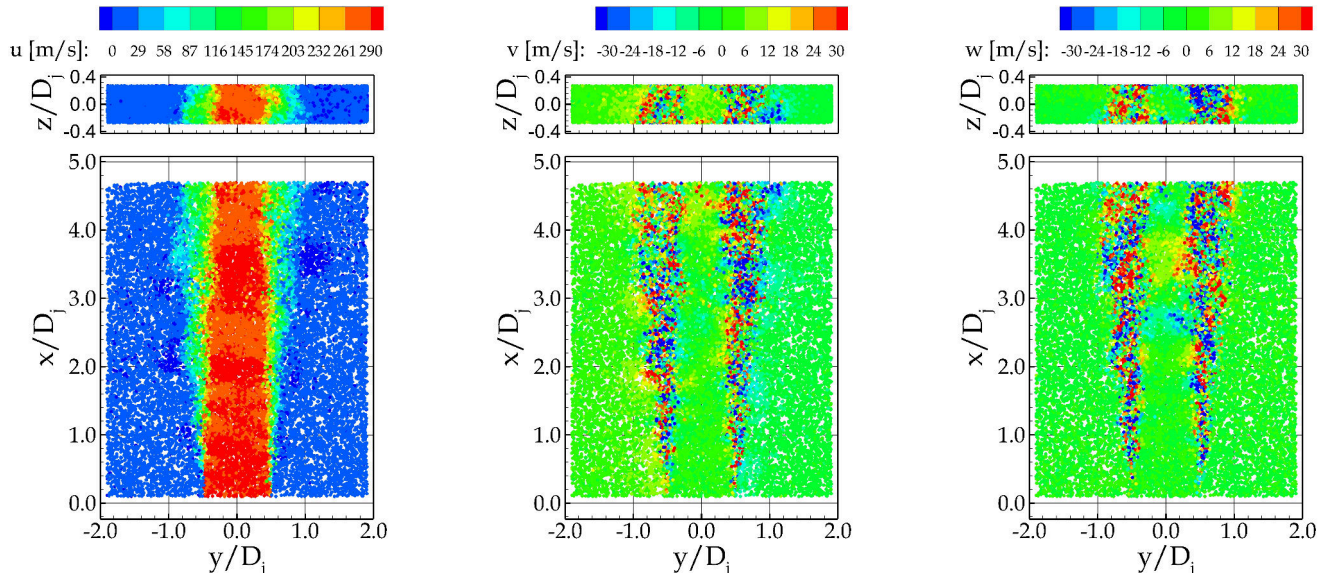

Figure 6: Instantaneous scatter plots of each velocity component for M 0.845 jet.

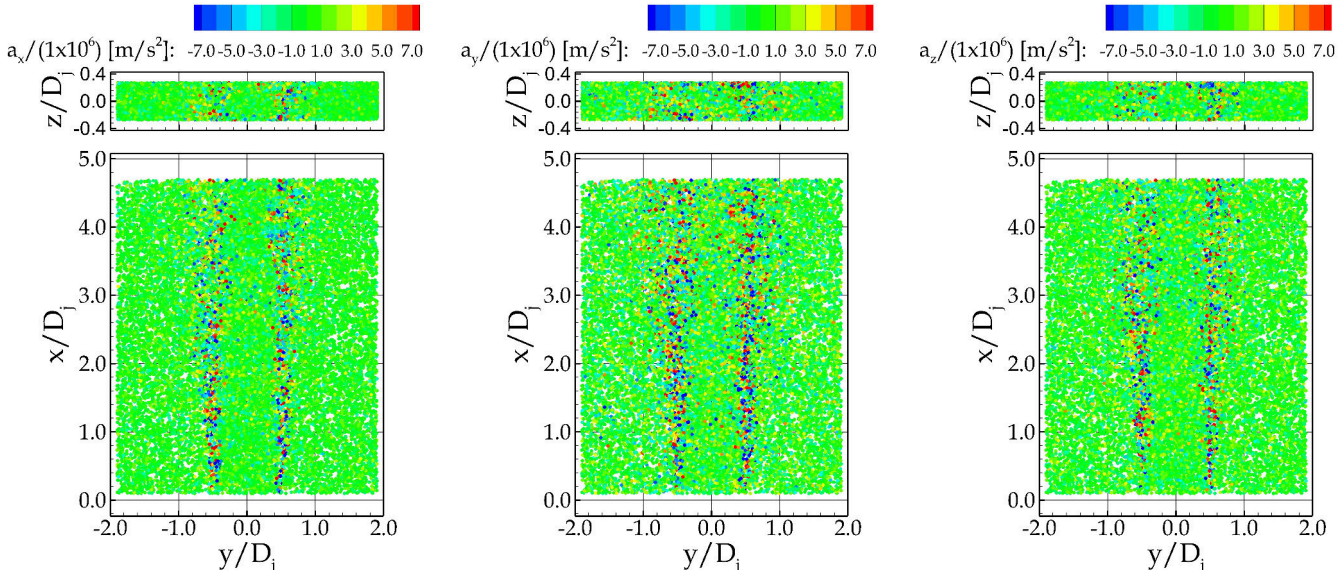

Figure 7: Instantaneous scatter plots of each acceleration component for M 0.845 jet.

flow fields and high resolution velocity statistics for the round jet at M 0.506 and M 0.845 are presented in Section 4.2 and 4.3, respectively. Subsequently, acceleration profiles and PDF statics are shown in Section 4.2.

A small cubic volume of 1 mm^3, centred in the middle of the jet core was used to obtain the jet exit conditions (Table 2). Bin-averaging of this volume over the complete data set provided sufficient samples (≈50,000) for convergence. The bin-averaging also revealed small velocity components in the y and z directions. These y and z components, were then used to transform the co-ordinates of each track such that x axis was aligned with the axial flow direction. After performing the transformation, the jet exit conditions were obtained and the velocity components in the y and z direction at the jet exit were zero.

4.1. Instantaneous flow field

For the case of M 0.845, Fig. 6 and Fig. 7 show scatter plots of instantaneous four-pulse tracks colour-coded by the flow velocity and acceleration components, respectively. Due to the slightly lower seeding density used for this specific recording configuration, the number of tracked particles is approximately 38,000 and was selected due to interesting features that are described below. The potential core region is clearly evident and extends past the measurement field. Small bands of axial velocity greater than 290 m/s (U_j) are evident inside the potential core of the jet. Also evident are small strands of higher levels of lateral (v) and out-of-plane (w) velocities that penetrate inside the potential core region. The jet shear layer is evident as a region of high lateral and out-of-plane velocities and accelerations. The layer is very thin near the nozzle exit, but quickly widens with increasing axial distance. Instantaneous

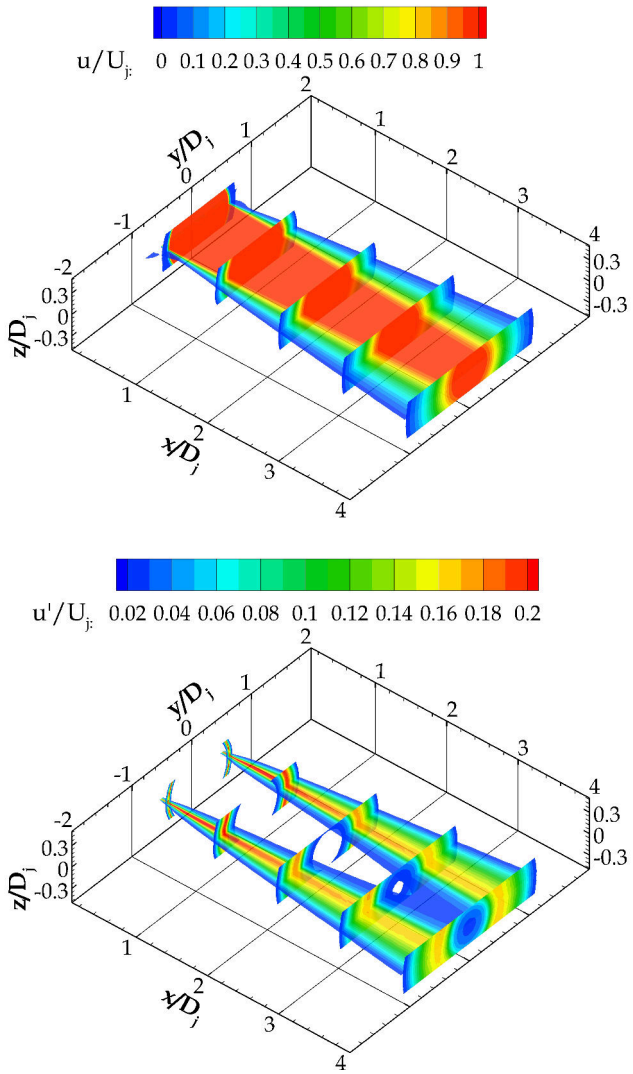

Figure 8: M 0.506 jet flow with streamwise slice at $z/D_j = 0$ and cross-stream slices at $x/D_j = 0.2$, 1, 2, 3, 4. Top: normalised mean axial velocity (u/U_j). Bottom: normalised axial component of turbulence intensity (u'/U_j).

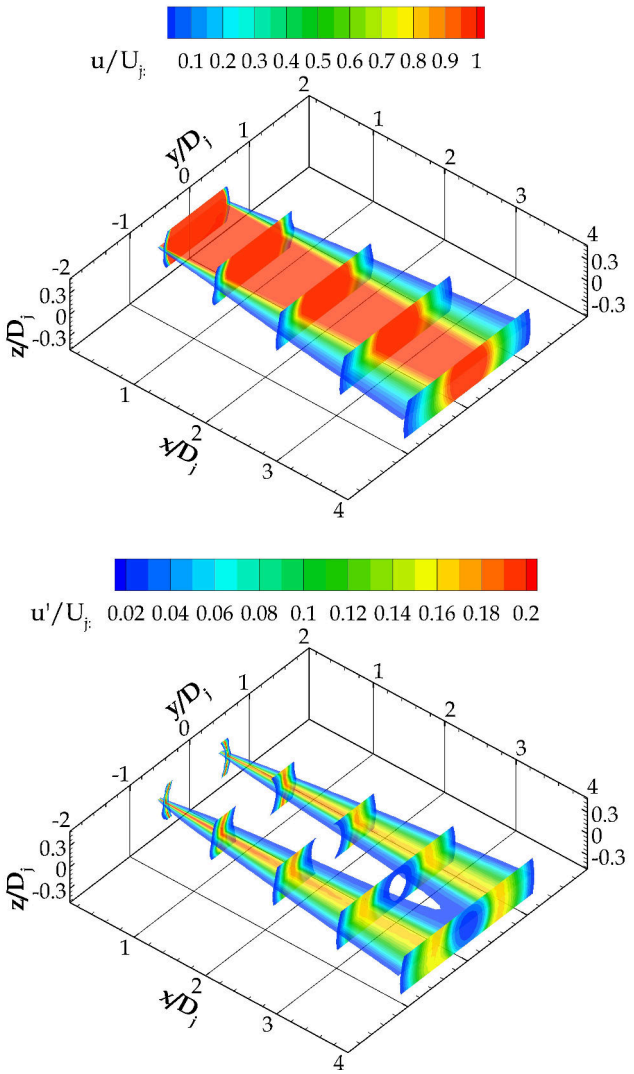

Figure 9: M 0.845 jet flow with streamwise slice at $z/D_j = 0$ and cross-stream slices at $x/D_j = 0.2$, 1, 2, 3, 4. Top: normalised mean axial velocity (u/U_j). Bottom: normalised axial component of turbulence intensity (u'/U_j).

accelerations greater than $7{\times}10^6$ m/s^2 are obtained in the shear layer of the jet. In the ambient region the track lengths are very small, the relative contribution of the position error is larger therefore producing noisier results. This is particularly evident in Fig. 7 for the lateral component of acceleration (a_y), with a small number of tracks in the quiescent region showing high levels of acceleration. These tracks make up less than 2% of the total number of tracks and are not observed in the velocity fields in Fig. 6.

4.2. *Mean flow field*

The mean (ensemble-averaged) flow field results are obtained by bin-averaging the scattered 3D particle track data into small volumetric bins. The bin-shape and size was tailored by taking into account the mean velocity gradients and number of available independent samples in order to obtain converged turbulence statistics. The rectangular bin size chosen here had the following dimensions, (δx, δy, δz) = (30 px, 10 px, 10 px). In order to resolve the high radial gradients in the shear layer smaller bin lengths were chosen whereas the lower velocity gradients in the axial direction allows the use of a larger bin length, thereby enabling a greater number of particle tracks to be collected.

Fig. 8 and Fig. 9 show the normalised axial velocity and axial component of turbulence intensity for M 0.506 and M 0.845, respectively. Each plot shows a streamwise slice at $z/D_j = 0$, and five cross-stream slices at axial locations, $x/D_j = 0.2$, 1, 2, 3, and 4. The colour contours represent the axial velocity component in the jet flow, where any velocity below $0.03{\times}U_j$ has been blanked in the plots to provide unobstructed viewing of the cross-stream flow planes. The turbulence intensity plots are also blanked below $0.03{\times}(u'/U_j)$. The results for both M

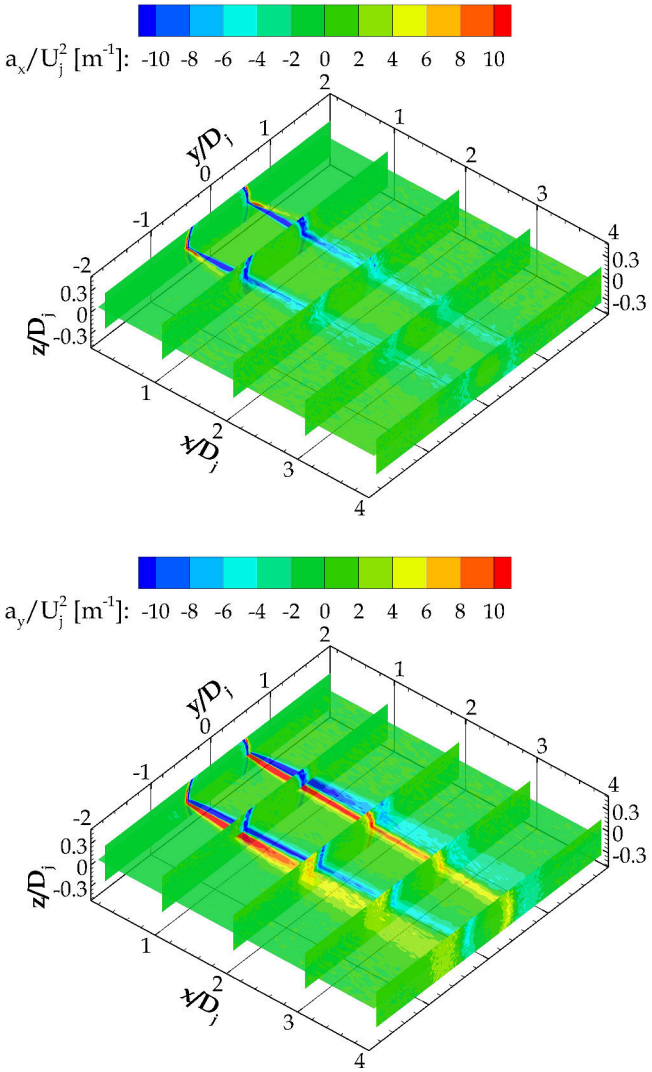

Figure 10: M 0.506 jet flow with streamwise slice at $z/D_j = 0$ and cross-stream slices at $x/D_j = 0.2, 1, 2, 3, 4$. Top: normalised mean axial acceleration (a_x/U_j^2). Bottom: normalised mean lateral acceleration (a_y/U_j^2).

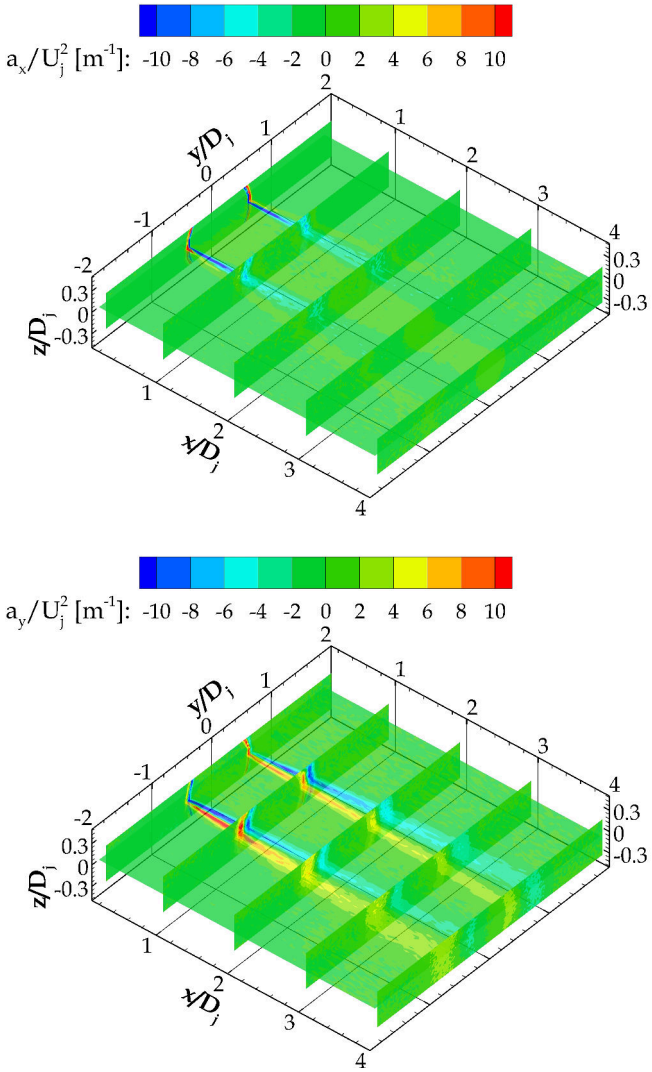

Figure 11: M 0.845 jet flow with streamwise slice at $z/D_j = 0$ and cross-stream slices at $x/D_j = 0.2, 1, 2, 3, 4$. Top: normalised mean axial acceleration (a_x/U_j^2). Bottom: normalised mean lateral acceleration (a_y/U_j^2).

0.506 and M 0.845 exhibit typical jet flow characteristics. The shear layer is very thin near the nozzle exit, but quickly widens with increasing axial distance, while the potential core narrows. Consistent with the literature the higher Mach number case features a potential core with a larger downstream extension. The slice at $z/D_j = 0$ for both Mach numbers shows good symmetry in the flow field, as does the cross-stream slices for M 0.506. Whereas the M 0.845 cross-stream slice at $x/D_j = 0.2$ and 1.0 (Fig. 9) shows minor asymmetries circumferentially in the shear layer.

The mean normalised axial and lateral acceleration flow fields are shown in Fig. 10 and Fig. 11 for M 0.506 and M 0.845, respectively. The shear layer region is evident by the high levels of acceleration. The outer shear layer near the jet exit lip line ($y/D_j = \pm 0.5$) shows the highest levels, and represents the ambient flow that is entrained and accelerated by the high-speed jet core. Whereas, the highest levels of deceleration (negative acceleration) are in the inner shear layer as the jet flow in the core is decelerated within a very thin region at the nozzle exit, which then broadens radially downstream. By the axial location of $x/D_j \approx 4$ for M 0.506 and $x/D_j \approx 3$ for M 0.845, the axial acceleration levels subside to that of the jet core and outer (ambient) flowfield. In Fig. 10 and Fig. 11 (bottom), the lateral accelerations in the inner shear layer are directed outwards away from the core, whereas in the outer layer, the lateral accelerations are directed towards the core, they are broader and more diffuse. The inward and outward (mean) lateral accelerations and axial decelerations can be explained by many downstream convecting vortices along the shear layer in which the acceleration vector always points to the centre of the (ring-like) vortex lines or the respective pressure minimum. This symmetric behaviour is reflected in both mean acceleration

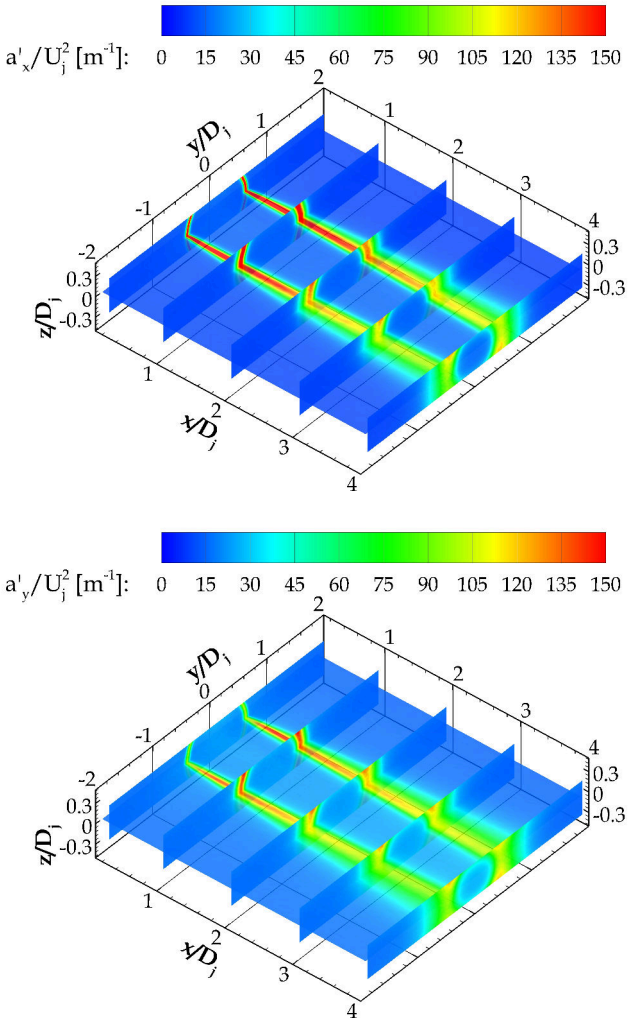

Figure 12: M 0.506 jet flow with streamwise slice at $z/D_j = 0$ and cross-stream slices at x/D_j = 0.2, 1, 2, 3, 4. Top: normalised axial acceleration fluctuations (a'_x/U_j^2). Bottom: normalised lateral acceleration fluctuations (a'_y/U_j^2).

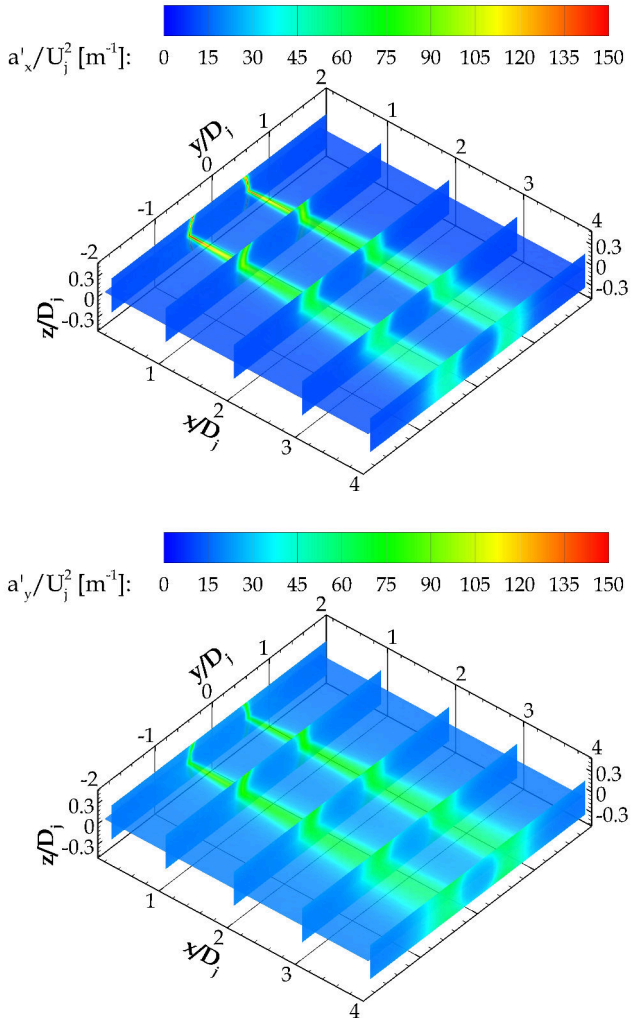

Figure 13: M 0.845 jet flow with streamwise slice at $z/D_j = 0$ and cross-stream slices at x/D_j = 0.2, 1, 2, 3, 4. Top: normalised axial acceleration fluctuations (a'_x/U_j^2). Bottom: normalised lateral acceleration fluctuations (a'_y/U_j^2).

fields. Higher levels of normalised acceleration are observed for M 0.506 and these high levels in the shear layer extend further downstream compared with the M 0.845 jet flow. This observation is consistent with the fact of a more extended potential core for the M 0.845 jet flow, or in other words a reduced normalised momentum exchange through the shear layers in the investigated volume.

The normalised fluctuations (standard deviation) of the particle accelerations are presented in Fig. 12 and Fig. 13, for M 0.506 and M 0.845, respectively. Peak acceleration fluctuations are 20 times greater than the maximum mean accelerations measured in the shear layer. The axial acceleration fluctuations are greater than the lateral accelerations for both Mach numbers and as with the mean accelerations, the M 0.506 case displays higher levels of fluctuations compared with M 0.845. In the outer region, upper and lower bounds of the volume in the z direction (z/D_j <-0.25 and z/D_j >0.25), some of the radial symmetry is lost and higher fluctuations are evident. The additional noise that is present here may be due to low dynamic range of the acceleration measurement and the lower light intensity at the border of the illuminated volume.

4.3. High resolution velocity statistics and effect of bin size

Contrary to cross-correlation based (e.g. PIV) methods, that are limited to a certain sub-region (or interrogation window) size, the resolution of bin-averaged approach, for a constant particle concentration, is primarily dependent on the total number of snapshots (images) and the volumetric bin size that provides sufficient statistical convergence of the samples within. The number of samples can be increased by increasing the number of snapshots recorded, thereby allowing the use of smaller bins down to sub-pixel resolution. In the previous section rectangular bins were used with the following dimensions, (δx, δy, δz) = (30 px, 10 px, 10px). The number of samples per bin ranged from 1,500 to 4,000 and was dependent on the local

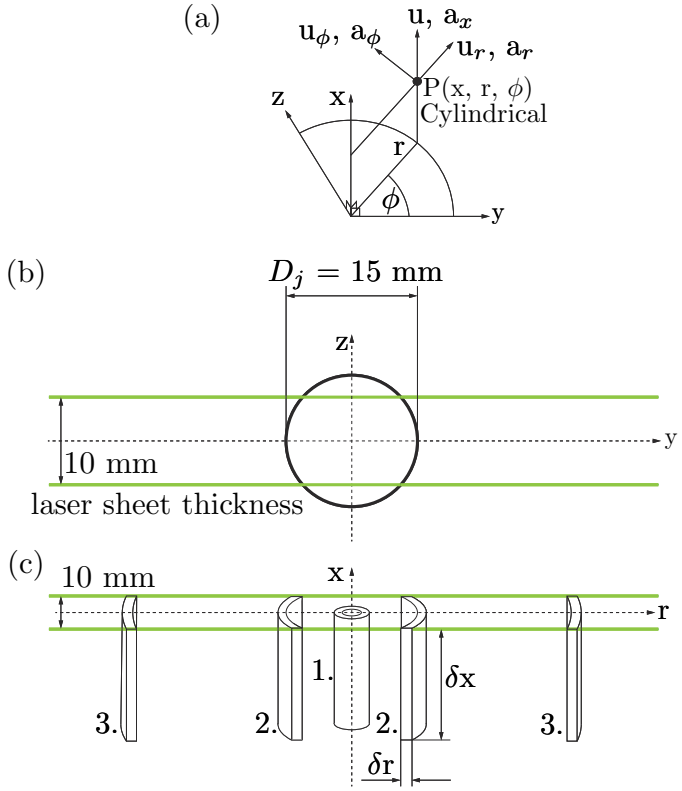

Figure 14: (a) Cylindrical co-ordinate system with respect to the Cartesian system. (b) Plan-view of the nozzle showing thickness of the laser sheet. (c) Three cylindrical shells (1., 2., 3.) with increasing radial diameters that are bound by the laser sheet thickness (green lines).

seeding and tracking density. The bin size was selected to resolve the local flow features and to ensure statistical convergence by having sufficient samples per bin. In order to obtain higher spatial resolution in the statistical flow quantities, we take advantage of flow symmetry and adopt a cylindrical co-ordinate system to provide bin-averaging in thin cylindrical shells (as shown in Fig. 14). The thin cylindrical shells are defined with the axial distance, δx as the height of cylinder, δr as the radial thickness (of the shell) and ϕ as the azimuthal angle. As shown in Fig. 14 (c), the cylindrical shells increase in diameter from the centre of the nozzle and are contained within the laser sheet thickness (i.e. -5 mm $\leq$ z $\leq$ 5 mm). Using the axial symmetry of the flow by setting $\phi = 360°$, at the centre of the jet a full cylinder is obtained (cylinder 1. in Fig. 14 (c)), as the diameter of the shells increases they are bound by the laser sheet thickness (as shown for cylindrical shells 2. and 3. in Fig. 14 (c)). This approach requires each track to be transformed so that the radial velocity and acceleration components (u_r, a_r), as well as the tangential velocity and acceleration components (u_ϕ, a_ϕ) are calculated, while the axial velocity and acceleration remain the same. The cylindrical shell bin-averaging method also requires an accurate known location of the jet centre which was confirmed by finding the centroid from the cross-stream plots in Figures 8 and 9. For this approach to be effective it is important that the jet centre remains stationary as the jet flow issues downstream (i.e. there is insignificant skewness in the jet flow). It is acknowledged that some spatial averaging may be evident due to instantaneous asymmetries in the jet flow, which may appear circumferentially and/or along the jet axis, however the large sample size helps to alleviate these effects.

The large sequence of recordings and using this approach allowed a cylindrical bin-size down to 20 px (0.59 mm or $0.04D_j$) in the axial direction and 0.75 px (23 μm or $0.0015D_j$) in the radial direction. For that case, 1,500 to 4,000 particles per bin were obtained. Results for an equal bin size of 5 px (0.15 mm or $0.01D_j$) in both the axial and radial directions were also obtained. Due to the larger volume for this case, the particle track numbers ranged from 5,000 to 25,000 per bin. In both cases, the cylindrical shells were ordered such that, in the potential core region they have similar volume; with larger radial spacing near the jet centre and then decreasing spacing until just before the jet shear layer is reached, where a constant radial spacing is used from that point on.

In the following section we compare the statical flow quantities from both the rectangular and cylindrical bin-averaging approaches. In Fig. 15 and Fig. 16, for M 0.506 and M 0.845, respectively, the radial profiles of the normalised mean axial velocity component (u/U_j) and axial turbulence intensity (u'/U_j) at axial stations $x/D_j = 0.2, 1.0, 4.0$ are presented. The experimental set-up and the implementation of the MP-STB technique allowed measurement close to the jet exit at $x/D_j = 0.2$. At that location, due to the high velocity gradients, the MP-STB results are shown for three different bin size resolutions. In that respect, the results for the rectangular bins of (δx, δy, δz) = (30, 10, 10) px and cylindrical bins with dimensions, (δx, δr) = (20, 0.75) px and (5, 5) px can be compared. It should be noted for the rectangular bins a central slice is made through the domain at $z/D_j = 0$, and so the lateral Cartesian co-ordinate is the same as the radial cylindrical co-ordinate (i.e. y = r and $v = u_r$). In Fig. 15 and Fig. 16, at $x/D_j = 0.2$ the step change in the axial velocity is captured well with the (30, 10, 10) px resolution rectangular bins but is better resolved with the (20, 0.75) px and (5, 5) px cylindrical bins. The shear layer at this location is extremely thin, as evident by the steep delta profile in the turbulence intensity (Fig. 15 and Fig. 16 – right). As a reference, the size of a typical PIV correlation window of 32 px is indicated in both figures. The delta profile appears to be well captured and resolved by MP-STB and the different bin-averaging approaches. There are however, small discrepancies in the peak values between the different approaches which may be partly attributed to the degree of spatial averaging within each volume. The M 0.845 jet flow, exhibits a greater asymmetry, in particular circumferentially near the jet exit (see Fig. 9), so the cylindrical bin averaging method averages over these asymmetries, resulting in lower peak values. Whereas, for the rectangular binning approach we take a central slice through the data without any radial averaging, therefore in this case producing a slightly higher peak value.

At $1\times D_j$ and $4\times D_j$, the results obtained from the present investigation are compared with the jet flow PIV consensus dataset (Bridges and Wernet, 2011). The jet flow conditions for the

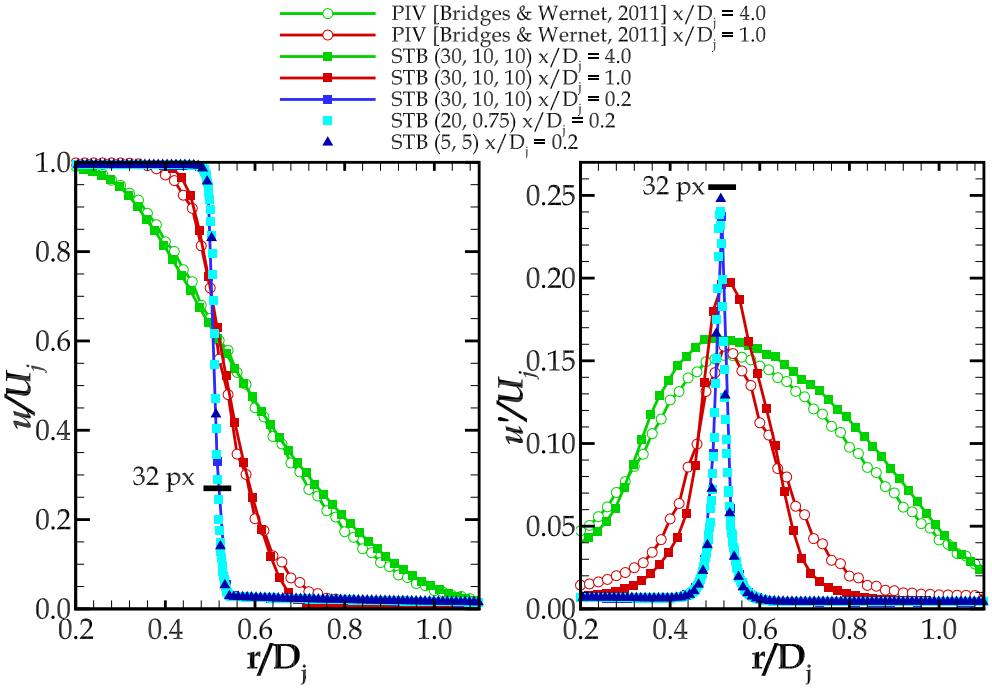

Figure 15: MP-STB results for M 0.506 jet. Left: radial profiles of normalised mean axial velocity component (u/U_j). Right: radial profiles of axial turbulence intensity (u'/U_j). The MP-STB bin-average resolution is indicated in px for rectangular bins (δx, δy, δz) or cylindrical bins (δx, δr). The PIV results are for M 0.5 (Bridges and Wernet, 2011), available for stations x/D_j = 1.0, 4.0. The size of a 32 px correlation window is given as a reference.

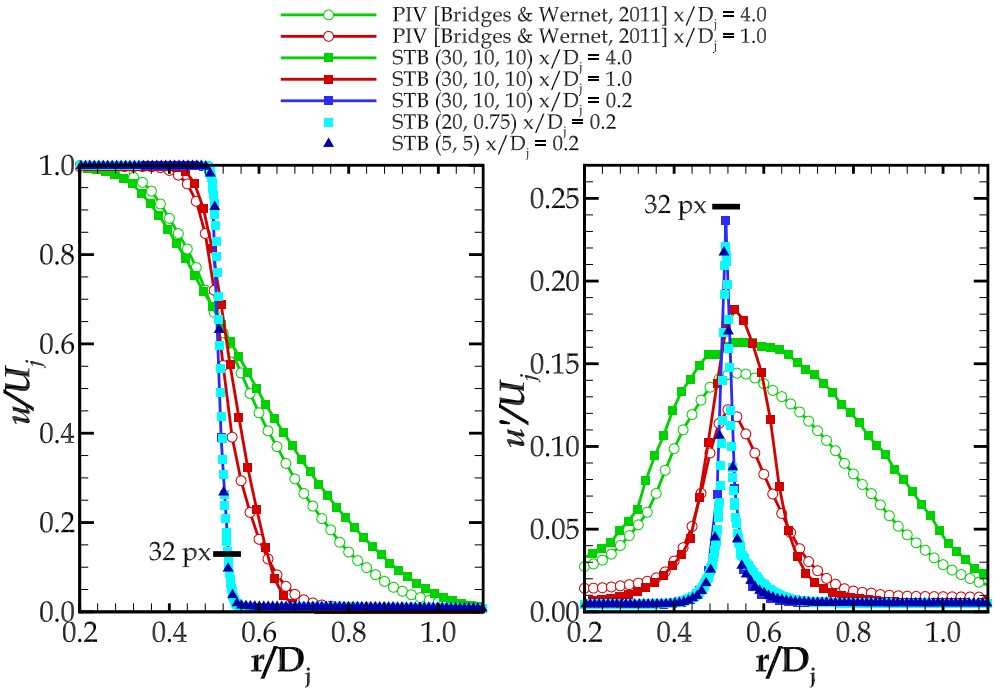

Figure 16: MP-STB results for M 0.845 jet. Left: radial profiles of normalised mean axial velocity component (u/U_j). Right: radial profiles of axial turbulence intensity (u'/U_j). The MP-STB bin-average resolution is indicated in px for rectangular bins (δx, δy, δz) or cylindrical bins (δx, δr). The PIV results are for M 0.9 (Bridges and Wernet, 2011), available for stations x/D_j = 1.0, 4.0. The size of a 32 px correlation window is given as a reference.

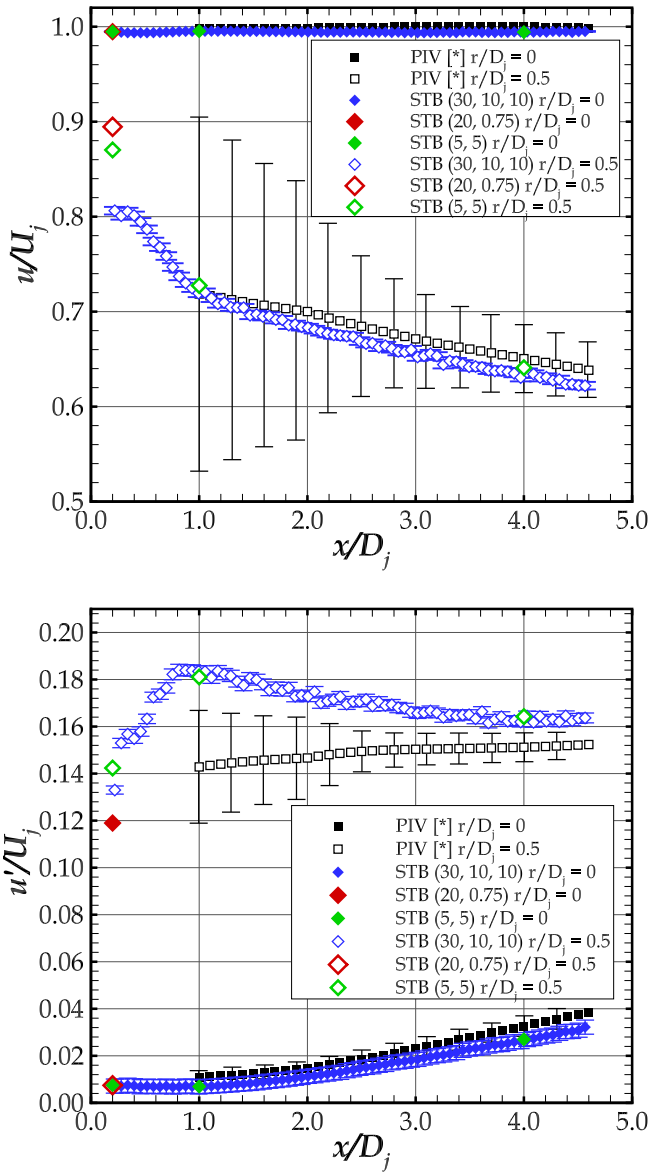

Figure 17: M 0.506 jet flow at the jet centre $r/D_j = 0$ and lip line, $r/D_j = 0.5$ compared with PIV at M 0.5 (*Bridges and Wernet, 2011). Top: normalised mean axial velocity (u/U_j). Bottom: normalised axial component of turbulence intensity (u'/U_j).

PIV data-set are as follows, for M 0.5, nozzle pressure ratio = 1.197, nozzle temperature ratio = 0.95, and $Re_{D_j} \approx 1.1{\times}10^6$ and for M 0.9, nozzle pressure ratio = 1.86, nozzle temperature = 0.835, and $Re_{D_j} \approx 1.1{\times}10^6$. The consensus data-set for these conditions was obtained by weighted averages from six historical PIV data-sets exploiting the axial symmetry. Despite slightly different test conditions compared to our cases, the consensus data-set provides a good reference for comparison. At $4{\times}D_j$ the profiles of axial velocity compare well, whereas for the turbulence intensity the MP-STB results show slightly larger turbulence intensities and a thicker shear layer. At $1{\times}D_j$ the benefit of the particle tracking approach over PIV (where the finite size of the cross-correlation windows results in a spatial averaging and modulation of the signal (Kähler et al., 2012b,a; Scharnowski et al., 2018)) is highlighted by MP-STB's capability of capturing the thin shear layer and the steep velocity gradients. The step change in the axial velocity component profile is better resolved with MP-STB. The turbulence intensity profiles are also well resolved and show greater intensity compared with Bridges and Wernet (2011); this may be attributed to the higher spatial resolution and accuracy of the Lagrangian particle tracking method where only a very small spatial averaging effect occurs within each bin compared to PIV (Kähler et al., 2012a; Scharnowski et al., 2018). Such discrepancies in PIV data have also been commonly reported in the study of turbulent boundary layers, where comparisons were made between PIV and DNS (Atkinson et al., 2013; Lee et al., 2016; Manovski et al., 2020). In all of these studies an underestimation of turbulence levels compared to DNS was primarily caused by the spatial averaging in PIV, due to the laser sheet thickness (in the case of 2D PIV methods) and the finite size of the interrogation windows. Furthermore, the LPT/PTV approach in principle is unbiased with respect to the amplitude of the velocity and acceleration fluctuation values because individual particles, at low Stokes numbers, can be assumed to be fluid elements contrary to the low-pass-filtered velocity fluctuations stemming from cross-correlation/PIV methods with finite sized windows. The effect of the boundary layer state at the nozzle exit on the downstream turbulence intensity distribution is another likely contributor to the discrepancy between the current results and that of the consensus data set. Several researchers have investigated these effects, and found significant differences in the turbulence levels, see Bogey et al., 2011; Fontaine et al., 2015; Brés et al., 2018; Bogey and Sabatini, 2019, and references therein. More recently, Bogey and Sabatini (2019) conducted Large Eddy Simulations (LES) of a M 0.9 jet at $Re_{D_j} = 5 \times 10^5$ to investigate the effects of different inflow conditions. In that study, they found that for an initially laminar boundary layer, the peak axial fluctuation was $0.174U_j$, whereas for a transitional and turbulent boundary layers, the peak values were lower, at $0.159U_j$ and $0.155U_j$, respectively.

As the test conditions for the MP-STB M 0.506 case and the PIV M 0.5 case are more closely matched a comparison is made for the normalised axial velocity and axial fluctuations along the jet axis in Fig. 17. The flow along the jet centre line, at $r/D_j = 0$ and jet lip line, at $r/D_j = 0.5$ are shown. Where useful in the comparison between data-sets, error bars are shown for MP-STB (see Appendix A) and PIV (see Bridges and Wernet, 2011). The MP-STB results are also shown for the different bin-averaging approaches and in the case of cylindrical bin-averaging, results are only shown at axial stations $x/D_j =$ 0.2, 1.0, 4.0. Along the jet centre line the MP-STB and PIV results compare very well for both the axial velocity and axial turbulence intensity. There is a small offset in the turbulence intensity along the jet centreline, which suggests that the jet in our study had slightly lower turbulence levels in the potential core. It should be noted that for the mean axial velocity the MP-STB error bars are significantly lower than the PIV error bars. At the lip line, the MP-STB axial velocity follows the general trend

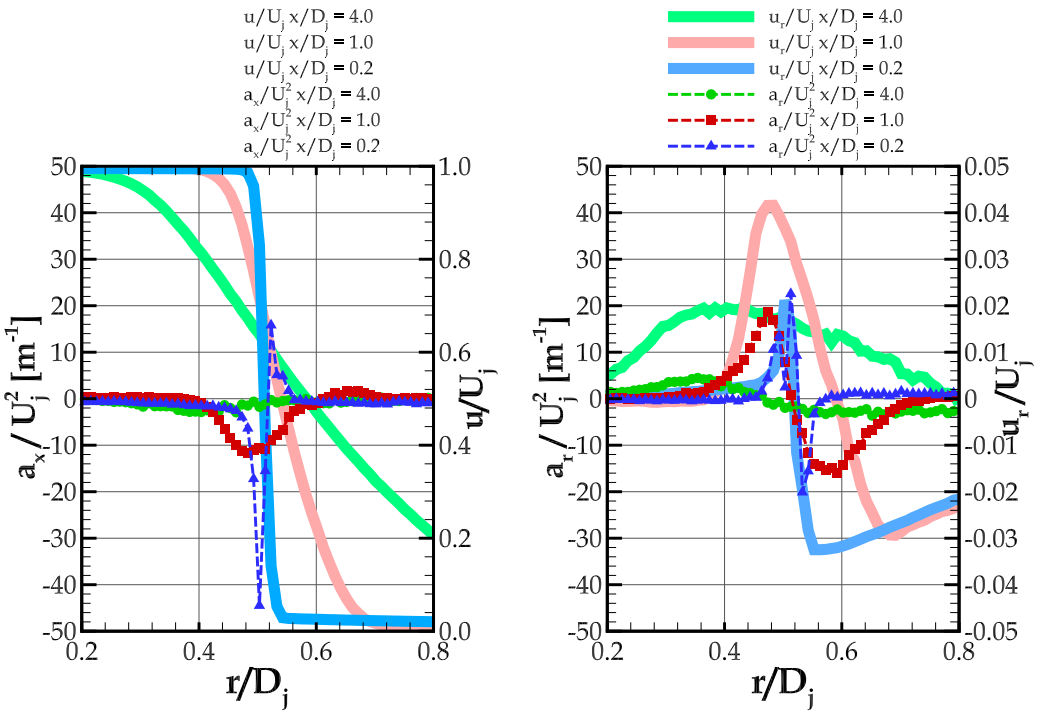

Figure 18: *M* 0.506 radial profiles of normalised acceleration and velocity. Left: axial component of acceleration and velocity. Right: radial component of acceleration and velocity.

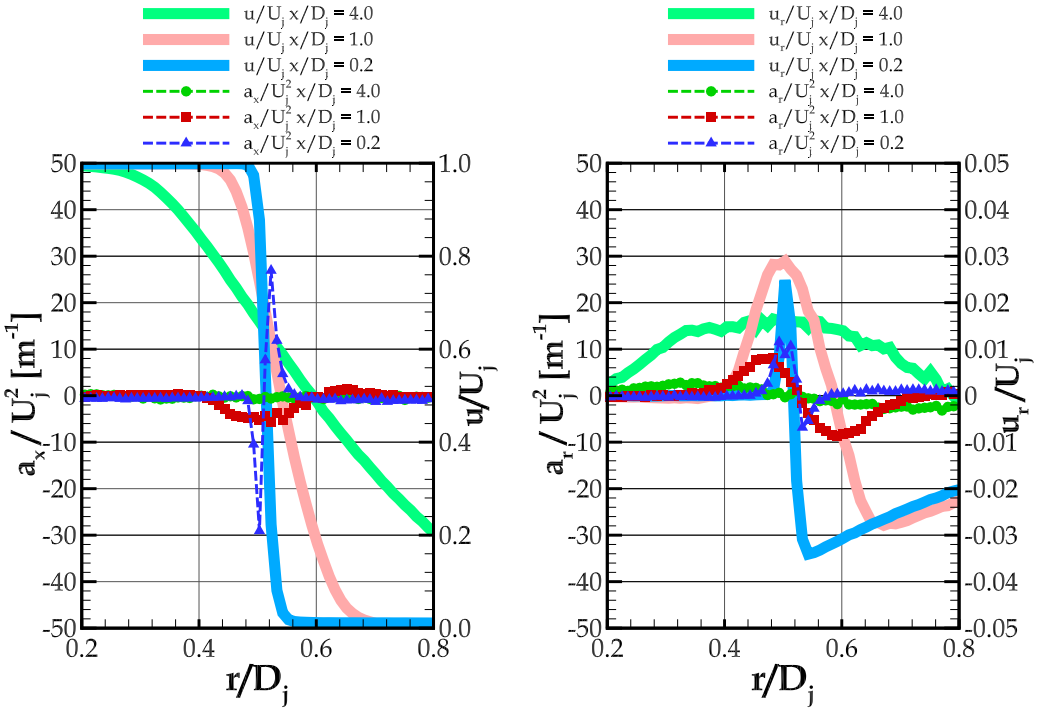

Figure 19: *M* 0.845 radial profiles of normalised acceleration and velocity. Left: axial component of acceleration and axial component of velocity. Right: radial component of acceleration and velocity.

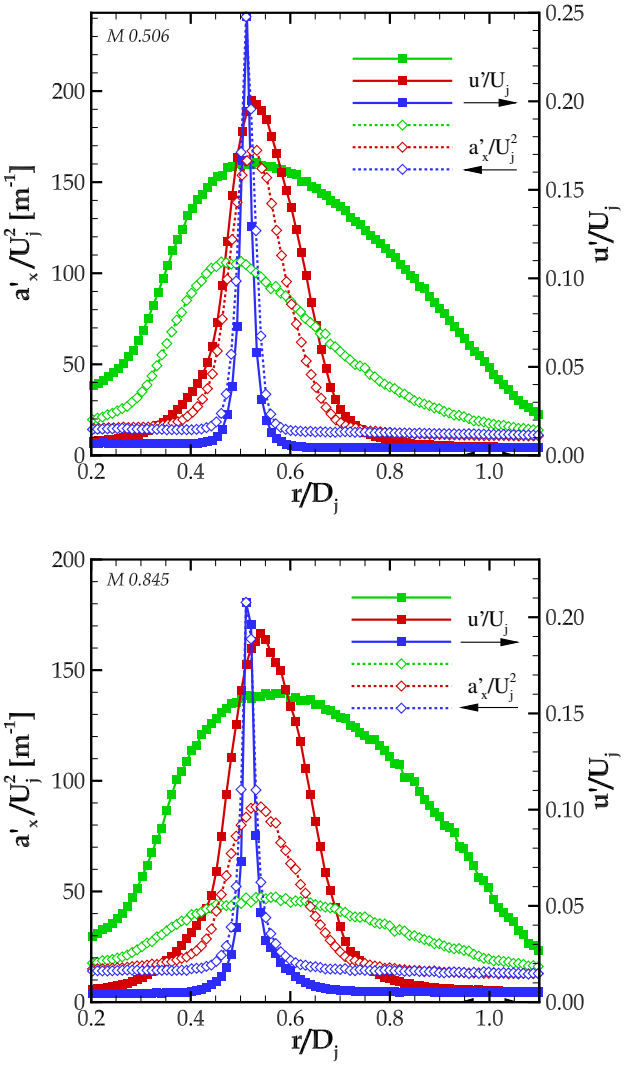

Figure 20: Fluctuations of axial acceleration (left axis) and axial velocity (right axis) at x/D_j = 0.2 (blue), 1.0 (red), 4.0 (green). Top: M 0.506 case. Bottom: M 0.845 case.

of the PIV results. The MP-STB rectangular and cylindrical bin-averaging approaches show similar results except at near nozzle location (x/D_j = 0.2). At this location the velocity gradients are very high and the larger rectangular bins show lower levels of normalised velocity due to spatial averaging within the larger bin size. As for the turbulence intensity at the lip line, the differences are more pronounced, MP-STB consistently shows higher levels along the jet axis. This comparison at the lip line is also very sensitive to the high velocity gradients in the radial direction (as evident in Fig. 15) and any asymmetries that may be present in the flow. In Fig. 17 for clarity purposes, the MP-STB error bars are only shown for the rectangular bin size of (30, 10, 10) px, whereas for the cylindrical bin-averaging of (5, 5) px the errors bars are approximately half the size due to the larger number of samples per bin.

The initial state of the boundary layer also plays an important role in the development of the shear layer fluctuations. In Bogey et al. (2011), LES was performed on a M 0.9 jet at a Re_{D_j} of 10^5, with a laminar boundary layer at the exit. Their results show axial velocity fluctuations with similar magnitudes and trend, to our results for M 0.845 (which are not plotted) but are akin to M 0.506 (in Fig. 17 – bottom). They suggest that the presence of a maxima shortly downstream of the nozzle exit may be indicative of strong mixing-layer transitions. They also made comparisons with experiments by Husain and Hussain (1979) in which the initial boundary layer was fully turbulent, those experimental results show lower turbulence levels that increase monotonically, similar to the PIV consensus data set. Our comparison above should thus be treated with appropriate level of caution as direct comparisons are only applicable for identical upstream conditions. These observations suggest that the boundary layer exiting our nozzle is likely either laminar or in a transitional state due to the higher levels of fluctuations, while the statements made above about the advantages of LPT over PIV are still valid. Future experimental and numerical investigations will be conducted to characterise the initial boundary layer state of the test nozzle.

4.4. Acceleration profiles and PDF statistics

One of the benefits of the Multi-Pulse STB Lagrangian particle tracking approach is that the material acceleration from individual tracked particles can be extracted. Profiles of the bin-averaged normalised axial and radial acceleration components are shown in Fig. 18 and Fig. 19, for both Mach numbers. The cylindrical shell bin size used in these results was (5,5) px and was selected due to the larger sample size ensuring better statistical convergence of the accelerations, which are constrained by lower dynamic range. The radial profiles for both Mach numbers show high levels of axial accelerations ($|a_x/U_j^2| > 20$) in the shear layer at the jet exit (x/D_j = 0.2) followed by much lower values downstream which then broaden. Furthermore, at x/D_j = 0.2 and 1.0 for both Mach numbers, the inner shear layer displays much greater decelerations compared to the positive axial acceleration in the outer layer. The radial accelerations show a more even distribution between the inner and outer layers due to the symmetry of the mean flow caused by vortices convecting along the shear layer. For M 0.506, the normalised accelerations in both the axial and radial components are higher than the M 0.845 case.

The axial velocity and acceleration fluctuations are compared in Fig. 20 for both cases. The right and left axes of both plots are scaled to match the peak values at x/D_j = 0.2. The profile shapes at x/D_j = 0.2 compare very well, however, downstream the axial acceleration fluctuations decrease more rapidly compared to the velocity fluctuations. In this plot, it is also apparent that for M 0.506, the normalised acceleration fluctuations are significantly larger than the M 0.845 case. At x/D_j = 4, the peak non-dimensional axial acceleration fluctuation $(a_x D_j/U_j^2)_{peak}$ is 1.6 and 0.73 for M 0.506 and M 0.845, respectively and is lower than the value of 2.4, reported by Brooks and Lowe (2014) for a heated supersonic jet at M 1.65 with a temperature ratio of 2. In that paper they measured the point wise fluctuating accelerations using Laser Doppler Velocimetry(LDV), and also investigated the self-similarity of the shear

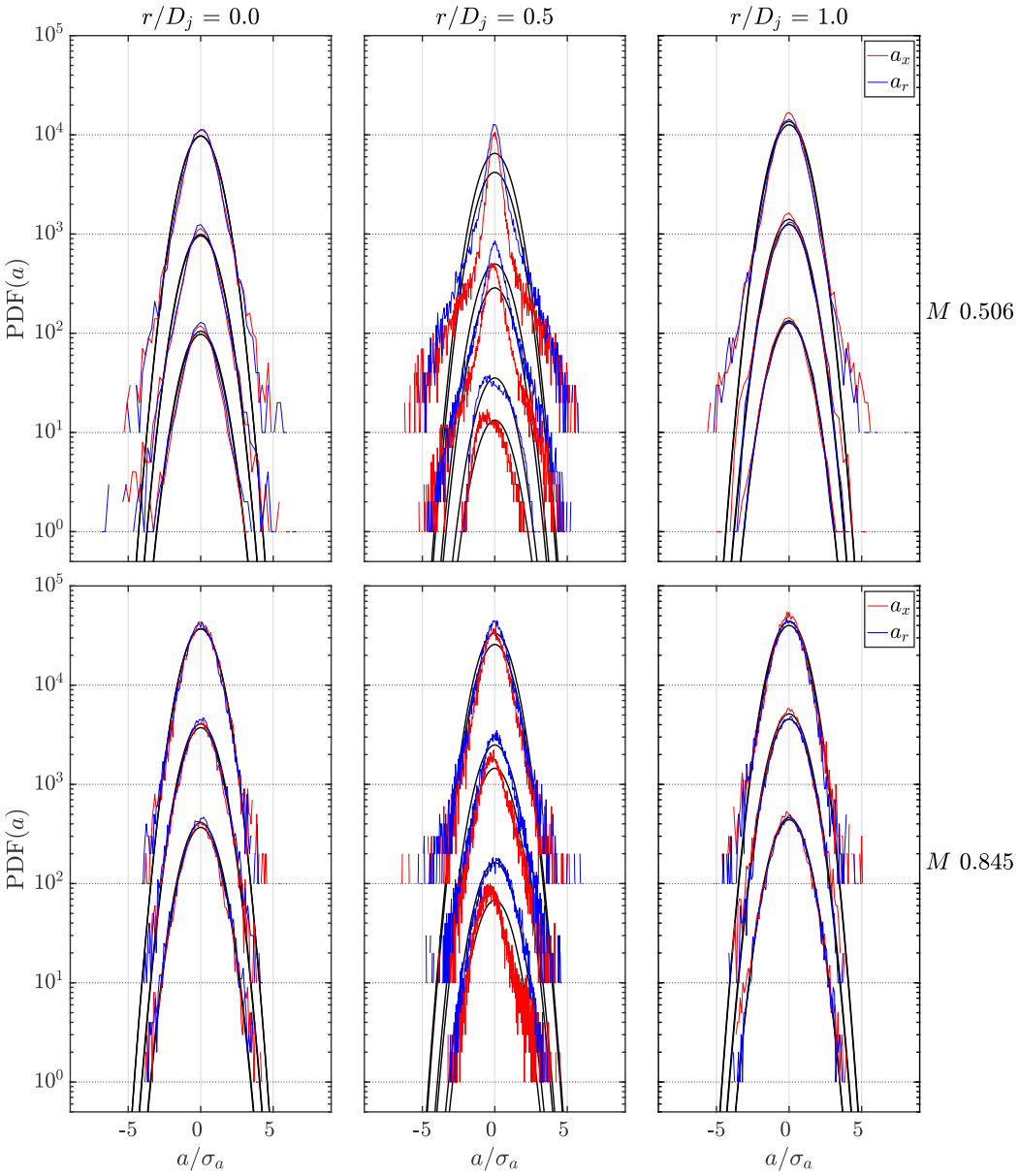

Figure 21: Probability distribution function (PDF) of normalised axial and radial accelerations based on cylindrical bin-averaging with size, (δx, δr) = (5, 5) px. The central positions of the bins are at x/D_j = 0.2, 1.0, 4.0 and the PDFs are shifted such that the lowest corresponds to x/D_j = 0.2. The black solid lines are Gaussian distributions for zero mean and the corresponding standard deviation (σ_a) of each cylindrical bin. Top: M 0.506 case. Bottom: M 0.845 case.

layer growth, which for our data can be a focus of future investigations.

Figure 21 shows the probability density function (PDF) of the non-dimensional axial and radial particle accelerations, at axial locations, x/D_j = 0.2, 1.0, 4.0 and radial locations, r/D_j = 0, 0.5 and 1.0. The PDFs are also obtained from cylindrical bin-averaging with (5, 5) px resolution. The PDFs are ordered such that the lowest profile corresponds to x/D_j = 0.2 and the other profiles are shifted by a factor of 10 for better clarity. The number of data points per bin range from 5,000 to 25,000. Also presented in each case as a reference is the Gaussian fit for zero mean and the corresponding standard deviation (σ_a) of each cylindrical shell. Mostly symmetric distributions are shown with wide tails, however the axial acceleration on the lip line near the jet exit shows some asymmetry. This asymmetry is towards negative values due to the overall deceleration of the exiting flow when interacting with the lower momentum fluid in the transitional and turbulent jet shear layer. At x/D_j = 4.0 for the radial locations r/D_j = 0 and 1.0, the distributions of acceleration are fairly symmetric and match the Gaussian fit well over the central peak but have wider tails. At the lip line, the distributions deviate from the Gaussian fit, with a higher peak and a wider tail, that continues to widen with axial distance. The radial location of r/D_j = 1.0 is in the quiescent region for

the first two axial locations, and follows the Gaussian fit closely, however at x/D_j= 4.0, which is located in the outer shear layer, the PDF shows a wider tail.

5. Summary of validation criteria

Identification and removal of outliers is well developed and robust in PIV, see Raffel et al. (2018) for example. In the present case a number of different strategies are used to validate the tracked particles. Firstly, the use of a velocity field predictor substantially reduces the likelihood of connecting a spurious track (Novara and Scarano, 2013). The PSC approach provides a robust quick initial predictor, however since high resolution statistics are desired, the resolution of the predictor also needs to be sufficiently high to resolve the velocity gradients in the flow, in particular the thin shear layer near the nozzle exit. Thus the final predictor used for processing of the complete sequence of recordings was obtained from a bin-average of a subset of STB particle tracks.

Secondly, further validation is achieved by the use of the iterative STB procedure with adaptive particle search radii based on the local velocity fluctuations in the flow. The iterative procedure allows for, initially a very restrictive, small search radii to be used, enabling only the most reliable tracks to be connected. Typically, for the first pass we obtain around 60% of the total particle tracks. In subsequent passes the adaptive factors ($f_{\sigma,2p}$ and $f_{\sigma,4p}$) are increased, allowing larger search radii to be used, while the probability of connecting a spurious track is reduced because of the presence of lower seeding densities in the residual images (i.e. due to the subtraction of already tracked particles). The variation in the track curvature is directly related to the standard deviation of the acceleration and the search radii could be adapted accordingly. Nevertheless, in our case we have used the velocity fluctuation due to the larger dynamic range and better accuracy. Further justification for this approach is that the high levels of velocity and acceleration fluctuations occupy very similar regions in the flow field, as evident from Figures 8, 9, 12, 13, and 20.

Thirdly, for each STB iteration each particle track is only accepted if the average deviation of the four particles in the track is below the allowed deviation (ε^*_{fit}) from a second order polynomial fit. This threshold value limits the allowable curvature of tracks and increases the chance that only valid tracks are connected. Again with the iterative approach, we start with a very restrictive small allowable deviation from fit and then with subsequent passes, the parameter is progressively relaxed (see Table 3) to allow higher curvature tracks to be connected. This approach has been successfully validated by Novara et al. (2016a) for measurement of a low speed turbulent boundary layer using a first order polynomial track fit and for simulated high subsonic base flow using a second order polynomial track fit (Novara et al. (2016b)). Overall with all three validation criteria applied, the percentage of discarded tracks was less than $\approx$ 2% of total tracks in both cases.

Additional criteria based on a median filter, with the velocity or acceleration of a track checked against neighbouring tracks within certain tolerance could be implemented. However, such filters were avoided as it may impose spatial averaging constraints to the data and the effectiveness of the filter would be heavily dependent on having sufficient local seeding density. As the MP-STB technique is relatively new, additional validation criteria measures are being tested or under development.

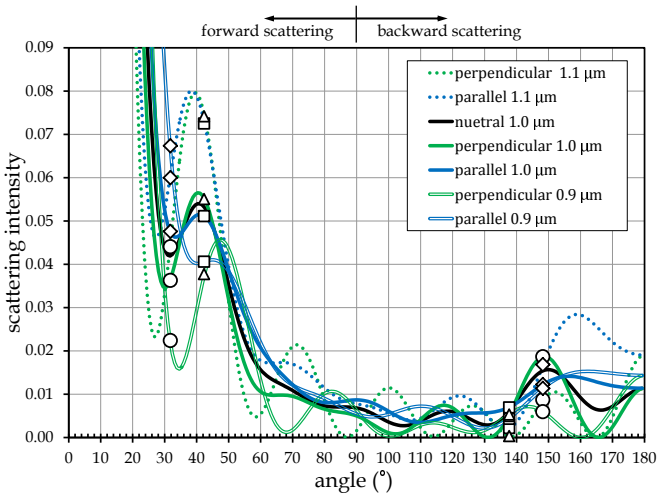

Figure 22: Angular scattering intensity for DEHS for particle sizes of 0.9 μm, 1 μm and 1.1 μm and different states of polarisation (neutral, perpendicular and parallel). The camera viewing angles for camera 1 and 3:◇, camera 5 and 7:□, camera 2 and 4:△, camera 6 and 8:○ are indicated for both the forward and backward scattering directions.

A sensitivity study was performed with the search radius multiplication factors as one parameter (since $f_{\sigma,4p}$ = 1.5 × $f_{\sigma,4p}$) and the deviation from fit parameter (ε^*_{fit}). To assess the sensitivity we used the number of successfully tracked particles. It was found that varying these parameters by ± 20% produced <2% change in the relative number of successfully tracked particles. For the current setup the sensitivity to these parameters is small, however such assessments should be conducted case by case.

6. Measurement sensitivity: analysis of particle images

For each camera the instantaneous images were analysed for the particle density and with a noise threshold of 40 counts the average number of particle peaks detected was approximately 80,000 (for an active sensor area of 1800×2200 px^2). The average number of particle peaks for each camera is summarised in Table 4. For some instances, the maximum number of particle peaks was up to 110,000 ($\approx$ 0.03 ppp). The number of particle peaks detected were not only dependent on the seeding density in the flow but also individual camera image quality. The worst performing cameras were 6 and 8, which typically found on average 66% of the number of particles peaks. The number of successfully tracked particles over the four pulses was lower still. An average of less than 50% of the number of particles in the flow were successfully tracked. The loss of particle images may be attributed to the different camera viewing angles resulting in significant variations in the image particle intensity along the four recordings due to the Mie scattering intensity

angular dependency, that is exacerbated by the different states of polarisation (Bohren and Huffman, 1983). A consequence of this, is that a particle that is visible for one imaging system may not be visible for the other, therefore failing to generate a complete track. Such instances will reduce the spatial resolution of the measurement and directly affect the iterative tracking approach of MP-STB. That is because, particle images that do not correspond to complete four-pulse tracks remain in the residual images and do not contribute to reducing the perceived seeding density for the subsequent STB iterations. This problem could also lead to an overall reduction of the accuracy in determining the particle position by means of IPR and affect the quality of the velocity and acceleration measurements (Novara et al., 2019). An assessment of this accuracy was made by analysing the 3D position of particle images from a zero-delay pulse tests where all lasers are fired simultaneously (see Appendix A for the uncertainty analysis). From the uncertainty analysis, the particle position accuracy between the two imaging systems of two different states of polarisation was found to be 0.23 px, whereas the position accuracy of each imaging system on their own (with light of the same polarisation state) was 0.13 px. The total position accuracy of the four-pulse tracks was determined to be 0.29 px. To further investigate the particle imaging performance of each camera, the expected theoretical Mie scattering behaviour for the current experimental arrangement is determined below.

Mie scattering theory states when light is incident on a sphere, its scattering and absorption characteristics are angular dependent and also dependent on the size of the sphere, the index of refraction and the polarisation of the incident light (Bohren and Huffman, 1983). Significant differences in the scattering behaviour are observed for unpolarised, parallel or perpendicular polarised light (Bohren and Huffman, 1983). The theory shows for small spherical particles the forward scattering direction (<90°) is highly peaked and narrow near 0°. The backward and perpendicular directions exhibit typically the lowest scattering intensity, generally more than 100 times less than the forward direction (near 0°). For spherical particles, if the incident light is 100% polarised to a particular plane the scattered light is also 100% polarised parallel to the same plane, that is, there is no cross polarisation (Bohren and Huffman, 1983). Whereas for unpolarised light the degree of linear polarisation for the scattered light is also angular dependent (cross polarisation occurs).

For the current experimental arrangement, the inner camera angles were approximately 31.8° from the x-y plane whereas the outer cameras were angled at 42.3°. The refractive index of DEHS is typically reported as 1.455 + 0.0i at 532 nm with the imaginary component (the index of absorption) reported as zero (Pettersson et al., 2004). Using these parameters the well-established Mie scattering calculator by Prahl (2016) was used. Prahl's algorithm is based on the code in Bohren and Huffman (1983), while being refined and validated based on recommendations in Wiscombe (1980).

Aerosol generators typically used for particle tracking (or PIV) in air produce a distribution of particle sizes that is fairly narrow with a mean around 1 μm. Instead of using a distribution of particle sizes we look at a narrow range of sizes in this analysis. The angular dependent scattering intensity was therefore calculated for three different DEHS particle sizes (0.9 μm, 1 μm and 1.1 μm) and for the different states of polarisation (neutral, perpendicular and parallel). This analysis also assumes that there is no absorption or scattering within the volume of particles and neglects the small light losses from back reflection. The results are plotted in Fig. 22. The camera angles for both the odd and even camera systems are indicated for both the forward and backward scattering directions. The scattering intensity is normalised by the scattering intensity in the forward direction (0°). As the incident laser light is back reflected through the flow field using a flat mirror, the total intensity of a scattered particle can be estimated by adding the forward direction angles (i.e. 31.8° or 42.3°) with the corresponding backward scattering intensity angles (i.e.137.7° or 148.2°). For each camera and for the three different particle sizes the total scattering intensity (forward plus backward) is summarised in Table 5 along with the corresponding intensity normalised by the maximum total intensity observed for the three particle sizes chosen. From Table 5 it's clear that the inner cameras (6 and 8) perform the worst. For each of the three particle sizes, cameras 6 and 8, have the lowest relative intensity out of the four camera arrangements. For a particle size of 0.9 μm the total intensity for cameras 6 and 8 is 36% of the maximum scattering intensity. The results of the theoretical scattering intensity of each camera coincide very well with the average number of imaged particle peaks from the experiment (Table 4), where cameras 6 and 8 also performed the worst. Therefore from this analysis we confirm the reason for the large disparity in particle imaging between cameras and the resulting low percentage of completed tracks.

Figure 22 also shows the importance of back reflection to even out the scattering intensity. The different curves show that back reflection will work most effectively if angles between cameras and the laser incident axis are less than about 22°. In that case, the scattering in the forward direction will dominate and the variations between different camera angles and states of polarisation will then be negligible. However, a possible drawback would be the increase in the Scheimpflug angles, which may then comprise the particle image intensities due to limitations in the angular efficiency of camera sensors. Additionally, such small viewing angles (<22° or <44° total angle) may compromise the tomographic reconstruction accuracy, in particular in the depth direction (Scarano, 2013). Scarano (2013) shows that the quality of the tomographic reconstruction is maximised when the total angle (or the tomographic angular aperture) between cameras ranges 40°– 80°, with slightly better accuracy when the angle is between 60°– 80°.

Aerosol generators with a relatively narrow band of particle sizes are generally adequate for PIV. However, for a polarisation based imaging (and particle tracking) such a particle size distribution is problematic. As shown in Fig. 22 for the chosen three particle sizes, only a slight increase of size from 0.9 μm to 1.1 μm increases the number of undulations in the scattering intensity as well as the differences between the states of polarisation. With this information a priori, one may be able to

Table 4: For each camera the average number of particle peaks (using a threshold of 40 counts) and the percentage of imaged particle peaks.

camera number	1	3	5	7	2	4	6	8
average particle peaks ($\times 10^3$)	80.0	80.0	83.4	78.4	75.4	69.0	54.8	55.2
particle peaks as a percentage	96%	96%	100%	94%	90%	83%	66%	66%

Table 5: For each camera and three different particle sizes, the sum of scattering intensity (forward plus backward) and the scattering intensity normalised by the maximum value.

camera (polarisation) [camera angles]	particle size (μm)	sum of scattering intensity	normalised intensity %
camera 1 and 3	0.9	0.079	100%
(parallel)	1.0	0.060	76%
[31.8° 148.2°]	1.1	0.077	98%
camera 2 and 4	0.9	0.043	55%
(perpendicular)	1.0	0.060	76%
[42.3° 137.7°]	1.1	0.075	95%
camera 5 and 7	0.9	0.045	57%
(parallel)	1.0	0.058	74%
[42.3° 137.7°]	1.1	0.075	95%
camera 6 and 8	0.9	0.028	36%
(perpendicular)	1.0	0.055	70%
[31.8° 148.2°]	1.1	0.053	67%

optimise a camera configuration arrangement such as to obtain a more even scattering intensity for each camera, and therefore increasing the ability to track more particles.

Novara et al. (2019) recently published results with a comparison between different Multi-Pulse STB methods, including a polarisation strategy, a timing-based strategy both with two imaging systems and also a multi-exposed imaging approach with only one imaging system. In the instantaneous images, similar to this study the polarisation strategy could typically recover approximately 57% of actual tracks, whereas the timing-based strategy, the percentage of detected tracks rises to approximately 70%. The multi-exposed imaging approach with only one imaging system produced a significant increase of tracks with more than 90% successfully reconstructed. In Sellappan et al. (2020), a multi-exposed imaging approach was also adopted and the percentage of successfully tracked particles was 74% and 62% for M 0.31 and M 0.59 jet flows, respectively. Since both studies were for different flow and different experimental set-up, a direct comparison is not applicable, nonetheless their encouraging results suggest that the multi-exposed imaging approach has advantages. The drawback of the multi-exposed imaging method is the doubling in the particle image densities and increased reconstruction burden for a given number of tracks but on the other hand it would provide a much better chance to minimise the residual images.

7. Concluding remarks

Using MP-STB, velocity and acceleration particle tracks were measured on a subsonic jet at two Mach numbers (0.506 and 0.845). The experimental set-up and tracking approach have been described. Instantaneous results and high resolution flow statistics were presented, revealing 3D acceleration and fluctuation fields, as well as the PDF statistics. The instantaneous scattered particle tracks were averaged in small volumetric bins. Both volumetric rectangular and cylindrical shell bins were used, comparisons between them were generally consistent, although some differences were evident. The cylindrical bin-averaging allowed much higher resolution flow statistics down to sub-pixel (0.75 px or 23 μm) in the radial direction and were better able to resolve the jet flow features.

The advantages of the MP-STB method have been demonstrated. These include its high accuracy, high dynamic velocity range and high spatial resolution of statistical quantities. These advantages provided MP-STB with the ability to resolve extremely steep velocity gradients in the jet flow and resolve the very sharp delta profiles of turbulence intensity across the thin shear layer near the nozzle exit. The MP-STB technique showed minimal spatial filtering, yielding higher turbulence intensities compared with the filtered approach of PIV from reported studies with similar flow conditions. The MP-STB techniques also provided additional information, such as the instantaneous acceleration fields and acceleration statistical quantities.

Some of the disadvantages or drawbacks of the MP-STB method include the effort and complexity of the set-up. Additionally, the number of images required for high resolution statistical quantities are significant which increases the operational time to gather the data and then process it.

From the uncertainty analysis in Appendix A, the particle position accuracy between the two imaging systems of two different states of polarisation (i.e. perpendicular and parallel polarised light) was found to be worse than the position accuracy of each imaging system on their own (with light of the same polarisation state). This disparity was attributed to the particle imaging quality of individual cameras and the sensitivity to the light scattering of particles, which was shown to be highly dependent on the particle size, camera angles, and different states of polarised light. An assessment of the particle imaging quality of each camera found that two of the eight cameras suffered greatly from reduced scattering intensity, resulting in less imaged particles and a lower percentage of tracked particles. To obtain a more even scattering intensity one recommendation is to keep all camera angles below 22°, while using a flat mirror for back reflection of the laser light. However, such low angles may compromise the tomographic reconstruction accuracy. Al-

ternatively, by knowing the particle size distribution and plotting the expected scattering behaviour for different states of polarisation, it is plausible that an optimised camera arrangement can be found, while maintaining accuracy in the reconstruction.

Although the validated tracked particles were typically less than 50%, of the total imaged particles, their overall velocity accuracy is relatively high (compared to PIV), as was evident in the uncertainty assessment (Appendix A) and the comparisons with published PIV results of similar flow cases. In comparison with classical PTV approaches (as in Kim et al., 2016) the tracked particle counts for MP-STB are still at least an order of magnitude greater. From the uncertainty analysis (Appendix A) it was also evident that the position uncertainty contributed the most to the velocity and acceleration uncertainty, although the timing error was also significant. Further improvements in the accuracy of the velocity and acceleration measurements can be made by reducing these uncertainties. In particular, the position uncertainty between the different imaging systems can be improved by optimising the camera arrangement, or avoiding the polarisation strategy altogether and using either a timing approach or better still a multiple-exposed particle imaging approach as in Novara et al. (2019) and Sellappan et al. (2020). The timing uncertainty can be improved by higher accuracy timing units or implementing active feedback control or laser timing stabilisers that claim more precise timing.

As stated by Wernet (2016) with reference to Tomo-PIV, the usefulness of the MP-STB technique needs to be weighed up against the availability and cost of hardware, the time and effort required to set up the experiment and then process the data. The MP-STB method requires a high amount of precision in calibrating the imaging system and ensuring accurate timing of the laser pulses is critical. In particular, if acceleration measurements are desired, they are very sensitive to these input variables.

The measurement campaign provides a broad basis for further investigations of turbulent jet flow and noise generation. The rich amount of data captured allows for the evaluation of a multitude of additional flow statistics such as two-point correlations, elements of the turbulent kinetic energy balance or turbulent length scales. While the current evaluation already demonstrates ensemble statistics at very high bin resolutions, the recently developed functional binning (Godbersen and Schröder, 2020) approach provides an opportunity to achieve even better results. By using a fully continuous representation of each track instead of discrete evaluation at a limited number of points the maximum amount of information can be extracted thereby improving convergence of the statistical quantities. The method is well suited for this experiment as it is designed for situations where tracks are longer than the spatial bins, which is generally the case here, and allows to directly include uncertainty quantifications into the binning process. Future evaluations would therefore allow the analysis of flow statistics at even higher resolutions.

8. Acknowledgements

Peter Manovski would like to thank the DSTG leadership team, in particular Bruce Woodyatt for facilitating the opportunity to conduct this research abroad and thanks to DLR for being an incredibly generous host. Dr Depuru Mohan is grateful to Homerton College, University of Cambridge, for the award of a Junior Research Fellowship. Dr Depuru Mohan would also like to thank DLR Göttingen and the DAAD for the award of a DLR-DAAD Research Fellowship. The authors are also grateful to the following DLR staff members, Thomas Ahlefeldt, Tobias Kleindienst, Michel Wüstefeld, Carsten Fuchs, Hartmut Mattner, Dirk Otter, Stefan Haxter, Carsten Spehr and Daniel Ernst at DLR Göttingen for their support. The authors would also like to acknowledge and extend their appreciation to Matteo Giacobello and Charitha de Silva for review of the manuscript and suggestions provided.

References

Adrian, R., 1997. Dynamic ranges of velocity and spatial resolution of particle image velocimetry. Measurement Science and Technology 8, 1393–1398. doi:10.1088/0957-0233/8/12/003.

Alkislar, M.B., Krothapalli, A., Butler, G.W., 2007. The effect of streamwise vortices on the aeroacoustics of a Mach 0.9 jet. Journal of Fluid Mechanics 578, 139–169. doi:10.1017/S0022112007005022.

Arakeri, V.H., Krothapalli, A., Siddavaram, V., Alkislar, M.B., Lourenco, L.M., 2003. On the use of microjets to suppress turbulence in a Mach 0.9 axisymmetric jet. Journal of Fluid Mechanics 490, 75–98. doi:10.1017/S0022112003005202.

Atkinson, C., Buchmann, N.A., Amili, O., Soria, J., 2013. On the appropriate filtering of PIV measurements of turbulent shear flows. Experiments in Fluids 55, 1654. URL: https://doi.org/10.1007/s00348-013-1654-8, doi:10.1007/s00348-013-1654-8.

Bendat, J.S., Piersol, A.G., 2010. Random data; Analysis and measurement procedures: 4th Edition. John Wiley & Sons, Inc.

Bogey, C., Marsden, O., Bailly, C., 2011. Large-eddy simulation of the flow and acoustic fields of a Reynolds number 10^5 subsonic jet with tripped exit boundary layers. Physics of Fluids 23, 035104. doi:10.1063/1.3555634, arXiv:https://doi.org/10.1063/1.3555634.

Bogey, C., Sabatini, R., 2019. Effects of nozzle-exit boundary-layer profile on the initial shear-layer instability, flow field and noise of subsonic jets. Journal of Fluid Mechanics 876, 288–325. doi:10.1017/jfm.2019.546.

Bohren, C., Huffman, D., 1983. Absorption and Scattering of Light by Small Particles. John Wiley.

Brés, G.A., Jordan, P., Jaunet, V., Le Rallic, M., Cavalieri, A.V.G., Towne, A., Lele, S.K., Colonius, T., Schmidt, O.T., 2018. Importance of the nozzle-exit boundary-layer state in subsonic turbulent jets. Journal of Fluid Mechanics 851, 83–124. doi:10.1017/jfm.2018.476.

Bridges, J., Wernet, M., 2011. The NASA subsonic jet particle image velocimetry (PIV) dataset. Technical Report NASA/TM-2011-216807. NASA Glenn Research Center. URL: http://turbmodels.larc.nasa.gov/jetsubsonic_val.html.

Bridges, J., Wernet, M.P., 2012. Validating large-eddy simulations for jet aeroacoustics. Journal of Propulsion and Power 28, 226–235. URL: https://doi.org/10.2514/1.B34385, doi:10.2514/1.B34385, arXiv:https://doi.org/10.2514/1.B34385.

Brooks, D., Lowe, K.T., 2014. Fluctuating flow acceleration in a heated supersonic jet, in: 17th International Symposium on Applications of Laser and Imaging Techniques to Fluid Mechanics, Lisbon, Portugal.

Christensen, K., Adrian, R., 2002. Measurement of instantaneous Eulerian acceleration fields by particle image accelerometry: method and accuracy. Experiments in Fluids 33, 759–769. URL: https://doi.org/10.1007/s00348-002-0488-6, doi:10.1007/s00348-002-0488-6.

Coleman, H., Steele, W., 2009. Detailed Uncertainty Analysis: Designing, Debugging, and Executing an Experiment. John Wiley & Sons, Ltd. chapter 5. pp. 121–191. doi:10.1002/9780470485682.ch5.

Discetti, S., Ianiro, A., Astarita, T., Cardone, G., 2013. On a novel low cost high accuracy experimental setup for tomographic particle image velocimetry. Measurement Science and Technology 24, 075302. URL: http://stacks.iop.org/0957-0233/24/i=7/a=075302.

Elsinga, G.E., Westerweel, J., Scarano, F., Novara, M., 2011. On the velocity of ghost particles and the bias errors in tomographic-PIV. Experiments in Fluids 50, 825–838. URL: https://doi.org/10.1007/s00348-010-0930-0, doi:10.1007/s00348-010-0930-0.

Fleury, V., Bailly, C., Jondeau, E., Michard, M., Daniel, J., 2008. Space-time correlations in two subsonic jets using dual particle image velocimetry measurements. AIAA Journal 46, 2498–2509. URL: https://doi.org/10.2514/1.35561, doi:10.2514/1.35561, arXiv:https://doi.org/10.2514/1.35561.

Fontaine, R., Elliott, G., Austin, J., Freund, J., 2015. Very near-nozzle shear-layer turbulence and jet noise. Journal of Fluid Mechanics 770, 27–51.

van Gent, P.L., Michaelis, D., van Oudheusden, B.W., Weiss, P.É., de Kat, R., Laskari, A., Jeon, Y.J., David, L., Schanz, D., Huhn, F., Gesemann, S., Novara, M., McPhaden, C., Neeteson, N.J., Rival, D.E., Schneiders, J.F.G., Schrijer, F.F.J., 2017. Comparative assessment of pressure field reconstructions from particle image velocimetry measurements and Lagrangian particle tracking. Experiments in Fluids 58, 33. URL: https://doi.org/10.1007/s00348-017-2324-z, doi:10.1007/s00348-017-2324-z.

Gesemann, S., Huhn, F., Schanz, D., Schröder, A., 2016. From noisy particle tracks to velocity, acceleration and pressure fields using b-splines and penalties, in: 18th International Symposium on Applications of Laser and Imaging Techniques to Fluid Mechanics, Lisbon, Portugal.

Godbersen, P., Schröder, A., 2020. Functional binning: Improving convergence of Eulerian statistics from Lagrangian particle tracking. Measurement Science and Technology URL: https://iopscience.iop.org/article/10.1088/1361-6501/ab8b84/pdf.

Henning, A., Koop, L., Schröder, A., 2013. Causality correlation analysis on a cold jet by means of simultaneous particle image velocimetry and microphone measurements. Journal of Sound and Vibration 332, 3148 – 3162. doi:https://doi.org/10.1016/j.jsv.2013.01.027.

Huhn, F., Schanz, D., Gesemann, S., Dierksheide, U., van de Meerendonk, R., Schröder, A., 2017. Large-scale volumetric flow measurement in a pure thermal plume by dense tracking of helium-filled soap bubbles. Experiments in Fluids 58, 116. URL: https://doi.org/10.1007/s00348-017-2390-2.

Huhn, F., Schanz, D., Manovski, P., Gesemann, S., Schröder, A., 2018. Time-resolved large-scale volumetric pressure fields of an impinging jet from dense Lagrangian particle tracking. Experiments in Fluids 59, 81. doi:10.1007/s00348-018-2533-0.

Husain, Z.D., Hussain, A., 1979. Axisymmetric mixing layer: Influence of the initial and boundary conditions. AIAA Journal 17, 48–55. doi:10.2514/3.61061.

Kähler, C.J., Kompenhans, J., 2000. Fundamentals of multiple plane stereo particle image velocimetry. Experiments in Fluids 29, S070–S077. URL: https://doi.org/10.1007/s003480070009, doi:10.1007/s003480070009.

Kähler, C.J., Scharnowski, S., Cierpka, C., 2012a. On the resolution limit of digital particle image velocimetry. Experiments in Fluids 52, 1629–1639. URL: https://doi.org/10.1007/s00348-012-1280-x, doi:10.1007/s00348-012-1280-x.

Kähler, C.J., Scharnowski, S., Cierpka, C., 2012b. On the uncertainty of digital PIV and PTV near walls. Experiments in Fluids 52, 1641–1656. URL: https://doi.org/10.1007/s00348-012-1307-3, doi:10.1007/s00348-012-1307-3.

Kim, J.T., Zhang, Z., Liberzon, A., Zhang, Y., Chamorro, L., 2016. On the Lagrangian features of circular and semicircular jets via 3D particle tracking velocimetry. Experimental Thermal and Fluid Science 77, 306 – 316. doi:https://doi.org/10.1016/j.expthermflusci.2016.05.003.

Lee, J.H., Kevin, Monty, J.P., Hutchins, N., 2016. Validating under-resolved turbulence intensities for PIV experiments in canonical wall-bounded turbulence. Experiments in Fluids 57, 129. URL: https://doi.org/10.1007/s00348-016-2209-6, doi:10.1007/s00348-016-2209-6.

Lynch, K.P., Scarano, F., 2014. Material acceleration estimation by four-pulse tomo-PIV. Measurement Science and Technology 25, 084005. URL: http://stacks.iop.org/0957-0233/25/i=8/a=084005.

Manovski, P., Jones, M.B., Henbest, S.M., Xue, Y., Giacobello, M., de Silva, C., 2020. Boundary layer measurements over a body of revolution using long-distance particle image velocimetry. International Journal of Heat and Fluid Flow 83, 108591. doi:https://doi.org/10.1016/j.ijheatfluidflow.2020.108591.

Miguel, E., Henning, A., 2013. Analysis of simultaneous measurement of acoustic pressure in the far-field and density gradient in the near-field in a cold jet, in: 19th AIAA/CEAS Aeroacoustics Conference.

Morris, S.C., 2011. Shear-layer instabilities: Particle image velocimetry measurements and implications for acoustics. Annual Review of Fluid Mechanics 43, 529–550. doi:10.1146/annurev-fluid-122109-160742.

Mullin, J.A., Dahm, W.J.A., 2006. Dual-plane stereo particle image velocimetry measurements of velocity gradient tensor fields in turbulent shear flow. part i: Accuracy assessments. Physics of Fluids 18, 035101. doi:10.1063/1.2166447, arXiv:https://doi.org/10.1063/1.2166447.

Novara, M., Scarano, F., 2013. A particle-tracking approach for accurate material derivative measurements with tomographic PIV. Experiments in Fluids 54, 1584. URL: https://doi.org/10.1007/s00348-013-1584-5, doi:10.1007/s00348-013-1584-5.

Novara, M., Schanz, D., Geisler, R., Gesemann, S., Voss, C., Schröder, A., 2019. Multi-exposed recordings for 3D Lagrangian particle tracking with multi-pulse Shake-The-Box. Experiments in Fluids 60, 44. doi:10.1007/s00348-019-2692-7.

Novara, M., Schanz, D., Gesemann, S., Lynch, K., Schroeder, A., 2016a. Lagrangian 3D particle tracking for multi-pulse systems: performance assessment and application of Shake-The-Box, in: 18th International Symposium on Applications of Laser and Imaging Techniques to Fluid Mechanics, Lisbon, Portugal.

Novara, M., Schanz, D., Reuther, N., Kähler, C.J., Schröder, A., 2016b. Lagrangian 3D particle tracking in high-speed flows: Shake-The-Box for multi-pulse systems. Experiments in Fluids 57, 128. doi:10.1007/s00348-016-2216-7.

van Oudheusden, B., 2013. PIV-based pressure measurement. Measurement Science and Technology 24, 032001. URL: http://stacks.iop.org/0957-0233/24/i=3/a=032001.

Perret, L., Braud, P., Fourment, C., David, L., Delville, J., 2006. 3-component acceleration field measurement by dual-time stereoscopic particle image velocimetry. Experiments in Fluids 40, 813–824. URL: https://doi.org/10.1007/s00348-006-0121-1, doi:10.1007/s00348-006-0121-1.

Pettersson, A., Lovejoy, E.R., Brock, C.A., Brown, S.S., Ravishankara, A.R., 2004. Measurement of aerosol optical extinction at 532 nm with pulsed cavity ring down spectroscopy. Journal of Aerosol Science 35, 995–1011.

Prahl, S., 2016. Mie scattering calculater version 2-3-5. Accessed 12 Sept. 2018. URL: https://omlc.org/calc/mie_calc.html.

Raffel, M., Willert, C., Scarano, F., Kähler, C., Wereley, S., Kompenhans, J., 2018. Particle Image Velocimetry: A Practical Guide. Experimental Fluid Mechanics. 3rd edition ed., Springer International Publishing.

Ragni, D., Schrijer, F., van Oudheusden, B.W., Scarano, F., 2011. Particle tracer response across shocks measured by PIV. Experiments in Fluids 50, 53–64.

Scarano, F., 2013. Tomographic PIV: principles and practice. Measurement Science and Technology 24, 012001.

Schanz, D., Gesemann, S., Schröder, A., Wieneke, B., Novara, M., 2013. Non-uniform optical transfer functions in particle imaging: calibration and application to tomographic reconstruction. Measurement Science and Technology 24, 024009. URL: http://stacks.iop.org/0957-0233/24/i=2/a=024009.

Schanz, D., Gesemann, S., Schröder, A., 2016. Shake-the-box: Lagrangian particle tracking at high particle image densities. Experiments in Fluids 57, 70. URL: https://doi.org/10.1007/s00348-016-2157-1, doi:10.1007/s00348-016-2157-1.

Scharnowski, S., Bross, M., Kähler, C.J., 2018. Accurate turbulence level estimations using PIV/PTV. Experiments in Fluids 60, 1. URL: https://doi.org/10.1007/s00348-018-2646-5.

Schröder, A., Schanz, D., Geisler, R., Willert, C., Michaelis, D., 2013. Dual volume and four-pulse tomo piv using polarized laser light, in: PIV13; 10th International Symposium on Particle Image Velocimetry, Delft, The Netherlands. Delft University of Technology, Faculty of Mechanical, Maritime and Materials Engineering, and Faculty of Aerospace Engineering.

Schröder, A., Schanz, D., Michaelis, D., Cierpka, C., Scharnowski, S., Kähler, C.J., 2015. Advances of PIV and 4D-PTV "Shake-The-Box" for turbulent flow analysis - the flow over periodic hills. Flow, Turbulence and Combustion 95, 193–209. URL: https://doi.org/10.1007/s10494-015-9616-2, doi:10.1007/s10494-015-9616-2.

Sciacchitano, A., Wieneke, B., 2016. PIV uncertainty propagation. Measurement Science and Technology 27, 084006. doi:10.1088/0957-0233/27/8/084006.
Sellappan, P., Alvi, F.S., Cattafesta, L.N., 2020. Lagrangian and Eulerian measurements in high-speed jets using Multi-Pulse Shake-The-Box and fine scale reconstruction (VIC#). Experiments in Fluids 61, 157. URL: https://doi.org/10.1007/s00348-020-02993-9.
Staack, K., Geisler, R., Schröder, A., Michaelis, D., 2010. 3D3C–coherent structure measurements in a free turbulent jet, in: 15th International Symposium on Applications of Laser and Imaging Techniques to Fluid Mechanics, Lisbon, Portugal.
Tinney, C.E., Glauser, M.N., Ukeiley, L.S., 2008. Low-dimensional characteristics of a transonic jet. part 1. proper orthogonal decomposition. Journal of Fluid Mechanics 612, 107–141. doi:10.1017/S0022112008002978.
Violato, D., Scarano, F., 2011. Three-dimensional evolution of flow structures in transitional circular and chevron jets. Physics of Fluids 23, 124104. URL: https://doi.org/10.1063/1.3665141, doi:10.1063/1.3665141, arXiv:https://doi.org/10.1063/1.3665141.
Violato, D., Scarano, F., 2013. Three-dimensional vortex analysis and aeroacoustic source characterization of jet core breakdown. Physics of Fluids 25, 015112. URL: https://doi.org/10.1063/1.4773444, doi:10.1063/1.4773444, arXiv:https://doi.org/10.1063/1.4773444.
Wernet, M., 2016. Application of Tomo-PIV in a large-scale supersonic jet flow facility. Experiments in Fluids 57, 144. doi:https://doi.org/10.1007/s00348-016-2228-3.
Wernet, M., 2017. Comparison of Tomo-PIV Versus Dual Plane PIV on a Synthetic Jet Flow. Technical Report. NASA/TM—2017-219508.
Wieneke, B., 2008. Volume self-calibration for 3D particle image velocimetry. Experiments in Fluids 45, 549–556. URL: https://doi.org/10.1007/s00348-008-0521-5, doi:10.1007/s00348-008-0521-5.
Wieneke, B., 2013. Iterative reconstruction of volumetric particle distribution. Measurement Science and Technology 24, 024008. URL: http://stacks.iop.org/0957-0233/24/i=2/a=024008.
Wieneke, B., 2017. PIV Uncertainty Quantification and Beyond. Ph.D. thesis. Delft University of Technology. doi:10.4233/uuid:4ca8c0b8-0835-47c3-8523-12fc356768f3.
Wiscombe, W.J., 1980. Improved Mie scattering algorithms. Applied Optics 19, 1505–1509. URL: http://ao.osa.org/abstract.cfm?URI=ao-19-9-1505, doi:10.1364/AO.19.001505.

Appendix A. Uncertainty and dynamic range of measurement

Simulations of particle flow fields with added noise levels (see van Gent et al., 2017) can be used to provide an estimate of the measurement uncertainty but all of the error sources cannot be correctly modelled to match real-world experiments. As pointed out by van Gent et al. (2017), experiments may contain many sources of error such as variability in seeding density, different camera viewing angles producing disparities in camera sensitivities and particle imaging, variations in the camera calibration throughout the volume, illumination with non-uniform intensity throughout the volume as well as variations from pulse to pulse, unwanted light reflections, lens effects and optical distortions due to the non-uniform index of refraction of the flow. All these factors contribute to a larger error in experimental data which are difficult to model. Thus to ascertain the measurement quality we compared the MP-STB results with well established 2C-PIV measurements and published data for similar flow cases. Additionally, in this section we estimate the uncertainty by considering only the main sources of error that contribute to the statistical uncertainty.

Velocity uncertainty

If we assume each of the samples are statistically independent and follow a normal distribution, the uncertainty in the ensemble averaged velocity measurement for a large sample size of N, can be estimated as

$$\frac{\varepsilon_{u,T}}{U_j} \simeq \sqrt{\frac{1}{N}\left[\left(\frac{\varepsilon_{u,r}}{U_j}\right)^2 + \left(\frac{\varepsilon_{u,b}}{U_j}\right)^2\right]}, \tag{A.1}$$

where $\varepsilon_{u,r}$ is the random (precision) uncertainty due to the unsteadiness of the flow (which is obtained from the standard deviation of the bin averaged statistics), and $\varepsilon_{u,b}$ is the bias uncertainty due to measurement accuracy of the MP-STB method.

Following Bendat and Piersol (2010) the uncertainty for the ensemble averaged turbulence intensity, is estimated by

$$\frac{\varepsilon_{u',T}}{U_j} \simeq \sqrt{\frac{1}{2(N-1)}\left[\left(\frac{\varepsilon_{u,r}}{U_j}\right)^2 + \left(\frac{\varepsilon_{u,b}}{U_j}\right)^2\right]}. \tag{A.2}$$

In the above expressions, we only consider the bias or systematic sources of error that contribute to the statistical uncertainty and disregard any other bias sources that are independent and more difficult to estimate. As such, we follow a similar PIV uncertainty approach to Sciacchitano and Wieneke (2016), who followed Coleman and Steele (2009) and assumed that each bias error whose sign and magnitude are known, have been removed by correction. Thus the remaining and main components of the bias uncertainty are assumed to be the calibration ($\varepsilon_{u,c}$), timing ($\varepsilon_{u,t}$) and position accuracy ($\varepsilon_{u,p}$),

$$\frac{\varepsilon_{u,b}}{U_j} \simeq \sqrt{\left(\frac{\varepsilon_{u,c}}{L_c}\right)^2 + \left(\frac{\varepsilon_{u,t}}{\Delta T}\right)^2 + \left(\frac{\varepsilon_{u,p}}{L_p}\right)^2}, \tag{A.3}$$

where each uncertainty is normalised by the following characteristic units, the jet velocity (U_j), calibration length (L_c), the overall pulse separation time (ΔT) and mean particle displacement over the jet flow field (L_p).

The calibration uncertainty of the cameras was obtained from the volume self-calibration analysis and the resulting disparity was 0.1–0.2 px in the measurement volume. The average value will be used for calibration uncertainty, $\varepsilon_{u,p} = 0.15$ px and is in general agreement with calibration errors obtained for Tomo-PIV (Scarano, 2013; Wieneke, 2017). Using a fast sensing light detector (Thorlabs DET10A/M) and an oscilloscope the pulse timing and pulse overlap between lasers was found to be within ±2 ns. Combining the timing error of the four pulses, produces,

$$\varepsilon_{u,t} = \sqrt{2^2 + 2^2 + 2^2 + 2^2} = \pm 4 \text{ ns},$$

for the complete sequence. For the position accuracy, a common method to quantify the uncertainty in four-pulse PIV experiments has been to image particles using a zero-time delay between pulses. After PIV evaluation of the images the displacement field should be zero and the resulting non-zero displacement has typically been documented as the uncertainty of the system (Christensen and Adrian, 2002; Perret et al., 2006; Lynch and Scarano, 2014). Lynch and Scarano (2014) performed this assessment on a 12-camera multi-pulse Tomo-PIV

system and demonstrated uncertainties below 0.2 voxel displacement for the u and v velocity components, and 0.4–0.6 voxel displacement, for the w-component (which was higher due to limited angular aperture in their set-up). In the current study, the zero-delay pulse tests were also used to quantify the position accuracy of the MP-STB algorithm between the two camera systems. The pulse configuration for these tests was such that all pulses were coincident for both volumetric systems (odd and even cameras, parallel and perpendicular polarised laser sources) and the images were acquired with lower particle image density. To quantify the displacement accuracy, the particles are initially triangulated from each camera system using IPR. Matched particles (i.e. the same particle evident for both imaging systems) are identified within a chosen threshold radius of 1.2 px and the resulting Euclidean distance (in 3D) was determined. The PDFs of the Euclidean distance in each component were found to be non-Gaussian positively skewed with a single peak and a long tail. The PDFs are very similar in profile to those obtained by Lynch and Scarano (2014) and in that study, the median value of displacement was chosen as the position accuracy. We also use the median value, but for our case we use the median Euclidean distance between matched particles for each pulse configuration as the position accuracy. Firstly, within the same imaging system the particle position accuracies were determined:

pulse 1-2: 0.13 px
pulse 3-4: 0.13 px.

For the last stage of the tracking process, when four-pulse tracks are connected (i.e. at the mid-point of the sequence) the position accuracy between the two imaging systems was determined:

pulse 2-3: 0.23 px.

For this particular camera configuration, the above represents the position accuracy for each of the three stages of the tracking process of the four-pulse sequence. For the total position accuracy of the four-pulse tracks we have to consider all three stages combined which is obtained by a root-sum-square approach:

$$\varepsilon_{u,p} = \sqrt{0.13^2 + 0.23^2 + 0.13^2} = 0.29 \text{ px}.$$

As expected, each imaging system produces identical position accuracy, whereas the position accuracy between the even and odd (camera numbers) imaging systems is higher and can be attributed to the anisotropic particle imaging (intensity variations) resulting from Mie scattering, due to the different states of polarised light, as was discussed in Section 6.

The particle position accuracies in each of the spatial directions were also determined and found to be lower than the Euclidean position accuracy. As the uncertainty assessment was not a prime focus of this study, a conservative approach was taken and the highest values corresponding to the Euclidean distance (in 3D) is reported. The Euclidean position accuracy relates to the velocity and acceleration magnitude of the measurement. Conservatively, the Euclidean position accuracy is assumed to be uniform across each of the spatial directions and subsequently the velocity and acceleration components. To further quantify the propagation of individual spatial accuracies to each of the velocity and acceleration components a thorough uncertainty assessment is required and will be subject of a future study.

The zero-pulse delay tests were conducted with and without jet flow. With high subsonic jet flows, high density gradients can potentially create additional sources of error due to changes in the index of refraction within the flow field resulting in different imaging properties of particles throughout the measured volume. Miguel and Henning (2013) performed Background Oriented Schlieren (BOS) as well as far field microphone measurements on the same nozzle (used in this study) for similar flow conditions and showed that the density gradients were strongest near the nozzle exit. As such, the particle position accuracies presented above were evaluated from particles images with jet flow. The position accuracy with the jet flow was slightly lower, confirming that the density gradients had a small influence on the overall imaging properties and the measurement uncertainty. Further analysis on the influence of the density gradients in the flow and the corresponding uncertainty throughout the measurement volume would be interesting but is out of scope of the current study.

The overall velocity bias error can now be determined from Eq. (A.3), where the calibration characteristic length is taken as the minimum thickness of the target, 12 mm (L_c = 404 px), as it is the shortest distance on the target and will provide the most conservative uncertainty. For M 0.506, the overall pulse separation time, ΔT = 11,250 ns. For the particle position accuracy, the characteristic length is considered to be the mean displacement (L_p = 40 px) over the jet flow domain, including the shear layer and potential core region. The bias uncertainty for M 0.506 is thus,

$$\frac{\varepsilon_{u,b}}{U_j} \simeq \sqrt{\left(\frac{0.15}{404}\right)^2 + \left(\frac{4}{11250}\right)^2 + \left(\frac{0.29}{40}\right)^2} = \pm 0.0074,$$

This bias uncertainty corresponds to a instantaneous velocity uncertainty of ≈1.3 m/s.

For a typical bin-averaged sample size of N = 3000, and using $\varepsilon_{u,r} \approx 0.10$ (the average standard deviation over the jet flow domain from the bin-averaged statistics) the uncertainties for the normalised mean velocity and turbulence intensity uncertainties from Eqs. (A.1) and (A.2) are ±0.0018 and ±0.0013, respectively. Similarly, for M 0.845, ΔT = 6,250 ns and $\varepsilon_{u,r} \approx 0.09$, this results in a bias uncertainty of ±0.0074, corresponding to a instantaneous velocity uncertainty of ≈ 2.2 m/s. The uncertainties for the normalised mean velocity and turbulence intensity for M 0.845 were estimated to be ±0.0016 and ±0.0012, respectively. The uncertainties above can be tailored for a specific location by using the local standard deviation of the velocity.

Following Adrian (1997), the dynamic velocity (DVR) range of the measurement can be estimated as the ratio between the maximum velocity magnitude within the investigated domain and the instantaneous velocity uncertainty. Wieneke (2017), from the analysis of various experimental investigations, found

that for Tomo-PIV, the average velocity bias errors (in displacement) ranged from 0.2 to 0.6 px. With a typical maximum particle displacement of 10–20 px the DVR is between 20 and 100 at best, for Tomo-PIV Wieneke (2017). In the instantaneous velocity uncertainty calculation for MP-STB above, the position accuracy is the most dominant term and so is the influence of the chosen characteristic length (L_p). If we choose the maximum particle displacement of 65 px as L_p we obtain a DVR of 224. Hence one of the main advantages of the MP-STB method is the improved accuracy and the ability to use larger displacements that result in a lower relative error and increased DVR, which is a significant improvement over Tomo-PIV.

Acceleration uncertainty

As per the equations below the acceleration is the second derivative of the quadratic fit to the four pulse particle positions,

$$position(\boldsymbol{s}) = c_1 t^2 + c_2 t + c_3, \tag{A.4}$$

$$velocity(\boldsymbol{u}) = \frac{d\boldsymbol{s}}{dt} = 2c_1 t + c_2, \tag{A.5}$$

$$acceleration(\boldsymbol{a}) = \frac{d^2\boldsymbol{s}}{d^2 t} = \frac{d\boldsymbol{u}}{dt} = 2c_1, \tag{A.6}$$

where c_1, c_2, c_3 are constants from the fit, t is time, $\boldsymbol{s}$ is the particle position(x, y, z), $\boldsymbol{u}$ and $\boldsymbol{a}$ are the velocity and acceleration total components, respectively. Due to the assumption that the position of the imaged particles follow a quadratic equation, the double differentiation results in a constant acceleration over the four pulse sequence.

Following a similar approach taken to estimate the velocity uncertainty, the normalised total mean ($\varepsilon_{a,T}$) and root-mean-square acceleration ($\varepsilon_{a',T}$) uncertainties may be written as

$$\frac{\varepsilon_{a,T}}{U_j^2} \simeq \sqrt{\frac{1}{N}\left[\left(\frac{\varepsilon_{a,r}}{U_j}\right)^2 + \left(\frac{\varepsilon_{a,b}}{U_j}\right)^2\right]}, \tag{A.7}$$

$$\frac{\varepsilon_{a',T}}{U_j^2} \simeq \sqrt{\frac{1}{2(N-1)}\left[\left(\frac{\varepsilon_{a,r}}{U_j}\right)^2 + \left(\frac{\varepsilon_{a,b}}{U_j}\right)^2\right]}, \tag{A.8}$$

where $\epsilon_{a,r}$ is the random (precision) acceleration uncertainty due to the unsteadiness of the flow (which is obtained from the standard deviation of the bin-averaged statistics), and $\epsilon_{a,b}$ is the bias acceleration uncertainty due to the MP-STB measurement method.

The bias uncertainty in the acceleration was estimated by considering the timing error for each pulse and the position errors as determined from the zero-pulse delay tests. For simplicity, the calibration uncertainty was neglected in this analysis and from the velocity uncertainty it's contribution was confirmed to be small. The average acceleration over the flow field (not including the ambient region) was used as the reference acceleration, along with the corresponding displacements for each pulse sequence. With these reference displacements, all combination of the timing uncertainty of each pulse (±2 ns) and the position accuracy (±0.13 px for the same imaging system and ±0.23 px between the two imaging systems) were considered and for each, the resulting 2^{nd} order polynomial fit was determined by least-squares regression. From Eq. (A.6) the acceleration was calculated and the maximum difference from the reference acceleration was determined, and is considered here as the estimated bias uncertainty in the acceleration measurement.

Using this method, for M 0.506 the normalised acceleration bias uncertainty was determined to be ±24.2 m^{-1}. For a typical bin-averaged sample size of N = 3000, the normalised standard deviation in the acceleration of the jet flow was ≈59.6 m^{-1}, and from Eq. (A.7) and Eq. (A.8) the resulting normalised uncertainty in the mean and acceleration fluctuation is ±1.12 m^{-1} and ±0.831 m^{-1}, respectively. For M 0.845, the normalised acceleration bias uncertainty was determined to be ±28.4 m^{-1}. Similarly, for N = 3000, the normalised standard deviation in the acceleration of the jet flow was ≈ 35.5 m^{-1}, and the resulting normalised uncertainty in the mean and acceleration fluctuation is ±1.81 m^{-1} and ±1.28 m^{-1}, respectively. Similar to the DVR, the dynamic acceleration range (DAR) is the ratio between the maximum measured instantaneous acceleration (typical for a four-pulse sequence) and the acceleration uncertainty. The DAR was determined to be 16 and 11, for M 0.506 and M 0.845, respectively.